Mineralogy and crystal chemistry of Mn, Fe, Co, Ni, and Cu in a deep-sea Pacific polymetallic nodule

Alain Manceau, Martine Lanson, Yoshio Takahashi

Mineralogy and crystal chemistry of Mn, Fe, Co, Ni, and Cu in a deep-sea Pacific polymetallic nodule

ALAIN MANCEAU[1,2,*] MARTINE LANSON[1,2] AND YOSHIO TAKAHASHI[3]

[1]Univ. Grenoble Alpes, ISTerre, F-38000 Grenoble, France.
[2]CNRS, ISTerre, F-38000 Grenoble, France.
[3]Department of Earth and Planetary Systems Science, Hiroshima University, 1-3-1 Kagamiyama, Higashi-Hiroshima 739-8526, Japan

* Corresponding author: Alain.Manceau@ujf-grenoble.fr
Running title: Mineralogy and crystal chemistry of a deep-sea nodule
Keywords: Mineralogy, XRD, SXRF, XANES, EXAFS, nickel, copper, vernadite, todorokite, birnessite, phyllomanganate, tectomanganate, ferromanganese nodule, polymetallic nodule, redox reaction.

ABSTRACT

Minor-element concentrations in marine ferromanganese nodules are primarily controlled by the mineralogy, which itself depends on redox conditions at the sediment-water interface. Results are presented for the first in-depth X-ray microstructural and microspectroscopic investigation of a mixed hydrogenetic-diagenetic nodule, which is representative of ferromanganese deposits on abyssal plains. The measurements were conducted by micro X-ray diffraction and X-ray absorption spectroscopy (both XANES and EXAFS) on hydrogeneous and diagenetic regions of the nodule. The hydrogenetic-diagenetic interface was imaged by X-ray microfluorescence, after which regions of interest were chosen to represent mineralogical and chemical transformations that occurred at the early stage of suboxic diagenesis. In the hydrogenetic nodule (oxic environment), Mn is speciated as Fe-vernadite, a nanocomposite material composed of intergrown feroxyhite (δ-FeOOH) and monodispersed phyllomanganate layers having no interlayer Mn (vernadite). In the diagenetic nodule (suboxic environment), Mn is speciated dominantly as Mg-rich 10Å-vernadite, which consists of a random intergrowth of vernadite and its transformation product todorokite. The authigenic 10Å-vernadite precipitated from the components of vernadite in Fe-vernadite that were dissolved in suboxic microenvironments of the sediment. Direct evidence supporting a redox-driven dissolution reaction is provided by the valence composition of Mn, as measured by micro-XANES, which is $0.69Mn^{4+}$ + $0.24Mn^{3+}$ + $0.07Mn^{2+}$ (average = 3.62 ± 0.04 v.u.) for Fe-vernadite and $0.61Mn^{4+}$ + $0.23Mn^{3+}$ + $0.16Mn^{2+}$ (average 3.28 ± 0.04 v.u.) for 10Å-vernadite. Nickel and Cu, derived mainly from dissolved vernadite and oxidized organic matter, replace structural $Mn^{3+/4+}$ in both the MnO_2 layer and todorokite domains of 10Å-vernadite. Pure todorokite in highly diagenetic regions of the nodule has an average formula of $Mg^{2+}_{0.167}(Mn^{4+}_{0.783}Mn^{3+}_{0.099}Co^{3+}_{0.002}Ni^{2+}_{0.076}Cu^{2+}_{0.040})O_2 \cdot nH_2O$, with an atomic ratio of

(Cu+Ni+Co)/Mn = 0.13 which is slightly lower than 0.167 (1/6), the maximum metal uptake capacity reported for marine nodules. By analogy with synthetic todorokites we infer that Mg^{2+}, which has a hydrated diameter close to that of the [3 x 3] tunnel, and Mn^{3+} and Cu^{2+}, which prefer Jahn-Teller distorted octahedra, play a crucial role in templating the topotactic transformation of 10Å-vernadite to todorokite and stabilizing todorokite in suboxic marine sediments.

INTRODUCTION

Sediments from oxygenated deep-sea plains often are covered with ferromanganese nodules that are characteristically rich in Ni, Cu and Li (Goldberg 1954; Usui 1979; Jiang et al. 2007). Mean concentrations of Ni, Cu, and Li in abyssal areas of greatest economic interest are about 1.1-1.3, 0.6-1.1, and 0.01-0.03 wt. %, respectively (Hein et al. 2013). Deep-sea nodules acquire their major (Fe, Mn), minor (Ni, Cu), and trace (Co, Pb, Ce) metals from two sources, seawater (hydrogenetic) and pore fluids (diagenetic) (Price and Calvert 1970; Piper and Williamson 1981). Diagenetic nodules are characterized by a high Mn/Fe ratio (typically > 2.5), Ni and Cu enrichment, and a mineralogy dominated by 10Å-manganates (Halbach et al. 1981; Lei and Boström 1995). In contrast, hydrogenetic nodules are lower in Mn, Ni, and Cu, but higher in Fe and trace metals, and their mineralogy is dominated by Fe-vernadite, an intergrowth of feroxyhite (δ-FeOOH) with monodispersed phyllomanganate layers (Burns and Burns 1975, 1979; Golden et al. 1986; Manceau and Combes 1988; Varentsov et al. 1991; Manceau et al. 1992). Although nodules occur that are solely hydrogenetic (e.g., on seamounts and sediment-free ridges) or diagenetic (e.g., in the southeastern Pacific) (Price and Calvert 1970), most show alternating micrometer laminae of the two genetic types (Margolis and Glasby 1973; Halbach et al. 1982). The rhythmic sequences of microlayers with different chemical and mineralogical characteristics are explained by variations of metal supply in the microenvironment of the accreting nodule surface. The hydrogenous component results from direct precipitation or accumulation of suspended nanoparticles from the bottom waters, whereas the diagenetic component results from oxic or suboxic diagenesis (Dymond et al. 1984). Under suboxic diagenetic conditions, such as are typical during microbial decomposition of organic matter, the redox potentials of the Mn^{4+}/Mn^{2+} and the Fe^{3+}/Fe^{2+} redox pairs lead to delayed dissolution of Fe oxides (e.g., feroxyhite) compared to Mn oxides (e.g., vernadite) (Lynn and Bonatti 1965; Calvert and Price 1977; Marchig and Gundlach 1981; Davison 1993). Divalent metal ions released from dissolution of Mn oxides diffuse upward in interstitial waters and reprecipitate under oxic diagenetic conditions at the sediment surface as 10Å-manganates around the accreting nodules. Redox-driven separation of Fe and Mn in suboxic sediments is a common post-accretional early diagenetic process also observed in shallow marine and lacustrine environments (Moore 1981; Tazaki 2000; Hlawatsch et al. 2001, 2002).

The structure and chemical composition of the manganese oxide phases covered in the term "10Å-manganates", and the crystal chemistry of incorporated trace metals, are long-standing questions of fundamental importance in marine mineralogy and geochemistry. We know from early electron microscopy observations that todorokite, a tectomanganate with [3 x 3] tunnel structure (Fig. 1) (Post and Bish 1988; Post et al. 2003), is the principal Mn mineral species in deep-sea nodules transformed

after deposition (Burns and Burns 1978a). Pure todorokite occurs typically in submarine hydrothermal fields (Usui et al. 1986) and late diagenetic nodules (Martin-Barajas et al. 1991). However, in most common early diagenetic nodules todorokite co-exists with buserite (Arrhenius and Tsai 1981; Ito et al. 1998), a phyllomanganate which also has a 10 Å *d*-spacing (Giovanoli et al. 1975). Buserite is a two-water (2W) layer hydrated form of the 7 Å mineral birnessite (Fig. 2) (Post and Veblen 1990; Kuma et al. 1994; Drits et al. 1997; Lanson et al. 2000). Synthetic buserite loses one water-layer (1W) and collapses to 7.1 Å at room temperature when it is exchanged with Na^+. When exchanged with Mg^{2+} or Ca^{2+}, synthetic buserite collapses only at 110 °C or in vacuum, a result of the higher ionic potential and greater negative enthalpy of hydration of small divalent cations (Paterson et al. 1986; Johnson and Post 2006). Terrestrial buserites, which generally contain a high proportion of Ca in their interlayer, collapse to 7.1 Å upon dehydration (Usui and Mita 1995; Manceau et al. 2007). Most intriguingly, mineralogical analyses of marine buserites show that they only partly collapse, which has been a source of uncertainty in their characterization (Burns et al. 1983; Lei 1996; Bilinski et al. 2002). This partial collapse could not be understood by X-ray diffraction (XRD), because the natural buserites are turbostratically disordered in the *c* direction (no *hkl* reflections), similarly to vernadite (Giovanoli, 1980; Chukhrov et al. 1987). For this reason and to be consistent with our previous terminology (Manceau et al. 2007), the terms 10Å-vernadite and 7Å-vernadite are used henceforth for randomly stacked buserite and randomly stacked birnessite, respectively. Note that the non-stoichiometric MnO_{2-x} nanosheets occur only as monolyayers in Fe-vernadite, which is the reason why this heterogeneous phase has no basal reflection in XRD.

The explanation for why marine buserites do not collapse completely is provided by high-resolution transmission electron microscopy (HRTEM). Images of natural todorokites show that the dimension of the tunnels is uniformly equal to three chains of edge-shared [MnO_6] octahedra in the [001] direction, as expected from the X-ray crystal structure, but is variable in the [100] direction ranging from double (T[3,2]) to nonuple (T[3,9]) octahedral chains (Fig. 1) (Chukhrov et al. 1979, 1985; Turner and Buseck 1979, 1981; Turner et al. 1982; Siegel and Turner 1983; Bodei et al. 2007; Xu et al. 2010). This observation has been linked to the loss of interlayer contractibility of marine buserite, and interpreted in terms of structural transformation during diagenetic reactions (Usui et al. 1989; Mellin and Lei 1993). In seawater, crystallographic rearrangement would begin with Mg-saturation of 10Å-vernadite and proceed gradually to ideal todorokite. Because the hydrated diameter of the Mg ions (8.6 Å) matches the nominal [3 x 3] tunnel size of todorokite, the Mg ions act as spacers between the pillars of the transforming octahedral sheets (Fig. 1). Thus, the Mg density in the [100] direction is essential in controlling the lateral width of the tunnels (Bodei et al. 2007). The amount of Mg^{2+} is a function of the layer charge, which itself depends on the extent of Mn^{3+} for Mn^{4+} substitution in the octahedral sheets. In addition, the Mn^{3+} cations, similarly to Ni^{2+} and Cu^{2+}, likely enhance the stability of todorokite by occupying the larger edge sites of the triple chains, and therefore also play a key role in the authigenic formation of todorokite (Burns et al. 1985; Post and Bish 1988; Post et al. 2003; Bodei et al. 2007; Cui et al. 2008).

Todorokite has been crystallized from a 10Å-phyllomanganate precursor in the laboratory (Golden et al. 1986; Feng et al. 2004; Cui et al. 2006). This does not mean, however, that all stable marine 10Å-manganates are either todorokite or pillared vernadites. Some authors consider that 10Å-vernadite is composed of two populations, one called "buserite-I" which transforms to 7Å-vernadite upon

dehydration, and another called "buserite-II" that contains a high amount of interlayer cations above vacancy sites which prevents this variety of phyllomanganate from collapsing to 7.1 Å (Fig. 2) (Novikov and Bogdanova 2007 ; Pal'chik et al. 2011). Yet another mineralogical complexity and source of confusion is the occurrence of asbolane and mixed-layer absolane-buserite as additional 10Å-manganates oxide phases in some marine ferromanganese concretions (Chukhrov et al. 1982, 1983; Manceau et al. 1992).

The crystal chemistry of Co, Ni, Ce, and Pb in marine ferromanganese oxides is generally well-known, in contrast to Cu which has not been explored. It is established that Co is trivalent and incorporated into the phyllomanganate layer of Fe-vernadite by replacement of Mn, whereas Pb is bound to both the Fe and Mn components of Fe-vernadite (Burns 1976; Takahashi et al. 2007). Cerium is tetravalent and also associated with the vernadite component, like Co (Takahashi et al. 2000), but how it is incorporated in the phyllomanganate structure is unknown, in contrast to Co (Manceau et al. 1997). Nickel is inside the MnO_2 layers of marine 7Å- and 10Å-vernadite, and also in the todorokite structure (Fig. 1, 3) (Bodei et al. 2007; Peacock and Sherman 2007a). Burns et al. (1985) postulated that Cu^{2+}, like Ni, occupies edge sites in todorokite. Copper also may be substituted for Mn in the vernadite layer, as suggested from Cu-sorption experiments on δ-MnO_2 (synthetic vernadite) conducted at pH 8 (Sherman and Peacock 2010).

The goal of this study is to better understand the hydrogenetic to diagenetic transformation through microscopic analyses of the chemical composition, mineralogy, and crystal chemistry of a deep-sea ferromanganese nodule. The nodule was examined previously and is representative of abyssal nodules altered by post-depositional remobilization of Mn relative to Fe accompanied by Ni and Cu enrichment (Takahashi et al. 2007). Here, the hydrogenetic-diagenetic interface was characterized at the micrometer scale using X-ray fluorescence (μ-SXRF), X-ray diffraction (μ-XRD), and X-ray absorption spectroscopy (both μ-XANES and μ-EXAFS). Manganese and Cu are the main focus of the XAS component of the present study. We used Mn-XANES to seek direct evidence for a redox signature of the transformation of diagenetic Fe-vernadite to 10Å-vernadite and todorokite. Mn-EXAFS was used to determine the local structure of Mn in Fe-vernadite, and Cu-EXAFS to determine the forms and crystal chemistry of Cu in the hydrogenetic and diagenetic parts of the nodule.

MATERIALS AND METHODS

Experimental sample synthesis

The synthesis procedure and characterization of the birnessite, vernadite (chemical and biogenic δ-MnO_2), and Co- and Ni-containing references were described previously (Manceau et al. 1997; Silvester et al., 1997; Villalobos et al. 2006; Bodeï et al. 2007; Grangeon et al. 2010). A set of Cu-sorbed phyllomanganates were synthesized at different pH, surface loading, and surface area (i.e., layer dimension) to enable the identification of the unknown uptake mechanism of Cu in the diagenetic nodule. The list of reference materials, their synthesis conditions, and the crystal chemistry of Cu within them, are summarized in Table 2. The surface area was varied by using well-crystallized birnessite (HBi and TcBi) and nanoparticulate δ-MnO_2 (dBi) as sorbents. The birnessite platelets have a lateral dimension of 1-2 μm (Tournassat et al. 2002) and the δ-MnO_2 particles 5-10 nm (Grangeon et al. 2012). In HBi, metal sorption is dominated by vacancies on the layer surface, which can be either

capped (TC complex) or filled (E complex) by the metal, and in δ-MnO_2 by vacancies and also edge sites at the layer edge owing to the small layer dimension (Manceau et al. 2007; Takahashi et al. 2007).

Deep sea ferromanganese nodule

The abyssal ferromanganese nodule D465 was collected at 5968 m water depth in a central Pacific sedimentary basin (location 09°03.40'N, 174° 04.10W) during the Hakurei-maru GH80-5 cruise expedition. The heterogeneous nodule consists of a hydrogenetic core surrounded by a diagenetic rim. The hydrogenetic-diagenetic interface was identified visually and two fragments, each one centimeter in length across the interface, were impregnated in resin. One sample was polished and carbon-coated for electron probe microanalysis (EPMA), and the other bonded to a glass slide, sectioned at a thickness of 30 microns, polished, and peeled off the glass substrate to facilitate transmission-mode μ-XRD. EPMA was performed with a JEOL JXA-8200, running at 15 keV acceleration voltage and using a 5 μm-sized beam. In backscattered electron imaging, the hydrogenetic-diagenetic interface shows numerous interspersed microlayers of each type of accretionary deposit and precipitates with a typical cauliflower-type growth pattern (Supplementary Fig. 1) (Halbach et al. 1982). Four regions, each about 1 mm in lateral dimension, were surveyed and 60 spots in hydrogenetic (opaque gray) and diagenetic (bright gray) regions were selected for analysis. Dark gray regions corresponding to clay phases were not analyzed. Major and minor element concentrations are given in Supplementary Table 1.

X-ray data collection and analysis

Synchrotron X-ray measurements were performed in air on the X-ray microprobe 10.3.2 at the Advanced Light Source (ALS) (Marcus et al. 2004). Three SXRF maps were recorded at a scanning resolution of 5 x 5 μm^2 (Map 1, 32373 pixels), 10 x 10 μm^2 (Map 2, 8775 pixels), and 15 x 15 μm^2 (Map 3, 32702 pixels), and a beam size adjusted from 10 x 7 μm^2 (Maps 2 and 3) to 5 x 5 μm^2 (Map 1), V x H FWHM, not to over-sample the data. The distributions of Ce, Mn, Fe, Co, Ni, Cu, and Pb were imaged by scanning the sample under a monochromatic beam and measuring the intensity of the Kα (Mn, Co, Ni, Cu), Kβ (Fe) and Lα (Ce, Pb) fluorescence lines with a 7-element Ge solid-state detector and a counting time of 100–500 ms per pixel. To eliminate fluorescence overlap, the intensities of the Ce(Lα), Co(Kα), and Pb(Lα) lines were measured by recording for each element one map above and another below their absorption edges (5730 eV and 5714 eV for Ce L_3-edge, 7731 eV and 7710 eV for Co K-edge, and 12985 eV and 13085 eV for Pb L_3-edge) and calculating the difference maps (Manceau et al. 2002b). The Fe(Kβ) radiation was measured below the Co K-edge to eliminate the Fe(Kβ) contamination by the Co(Kα) fluorescence. The fluorescence yield was normalized against the incident intensity I0 and the counting time. Elemental concentrations were calculated from EPMA, not from SXRF data because of the difficulties inherent to this type of quantification with X-rays.

From visual comparison of elemental distributions, points-of-interest (POIs) were selected for μ-XRD and X-ray absorption measurements at the Mn, Fe, Co, Ni, and Cu K-edges. Transmission-mode μ-XRD patterns were recorded with a Bruker 6000 CCD binned to 1024 x 1024 pixels at 17 keV incident X-ray energy and 16 x 7 μm beam size. The two-dimensional XRD patterns were calibrated with corundum (α-Al_2O_3) and integrated to one-dimensional patterns with the Fit2d code (Hammersley et al. 1996). X-ray absorption spectra were measured in transmission mode at the Mn and Fe K-edge

and in fluorescence-yield mode at the Co, Ni and Cu K-edges. To avoid possible radiation damage, only one spectrum was collected at each spot. Unless otherwise indicated, several single-scan spectra were recorded at distant spots having similar compositions and mineralogy, as seen on the SXRF maps and from μ-XRD patterns, and averaged.

Powder XRD patterns were recorded at ambient condition and in-vacuum with a Bruker D5000 diffractometer equipped with a Cu anode and a Kevex Si(Li) solid state detector. Samples were mounted in an Anton Paar TTK450 chamber attached to the diffractometer. A first pattern was recorded at ambient condition, then a second after in-situ dehydration realized by purging air for six hours with a turbomolecular pump. Some dehydrated samples were rehydrated in-situ in air at room temperature for several hours and a new pattern recorded.

RESULTS AND DISCUSSION

Chemical composition

EPMA analyses show a clear inverse relationship of Ni and Cu, on the one hand, and Co, Ce, and Pb, on the other hand, with the Mn/Fe ratio (Fig. 4). Ni and Cu concentrations increase sharply at Mn/Fe ~ 2.5, which divides purely hydrogenetic nodules from those that experienced the beginning of early diagenetic transformation (Halbach et al. 1981), and plateau above Mn/Fe > 10. The average concentrations are Ni = 0.37 (σ = 0.23) and Cu = 0.42 (σ = 0.18) wt. % in Mn/Fe < 2.5 regions (n = 26), and Ni = 3.06 (σ = 0.38) and Cu = 2.08 (σ = 0.37) wt. % in Mn/Fe > 10 regions (n = 12). In contrast, maximum amounts of Co, Ce, and Pb occur in hydrogenetic regions, where average concentrations are 0.24 (σ = 0.06), 0.09 (σ = 0.02), and 0.06 (σ = 0.02) wt. %, respectively. These elements average 1/3 to 1/2 these amounts in diagenetic regions, but fluctuations are large. The average EPMA results for the five trace metals coincide with previous chemical analyses of seafloor nodules (Piper and Williamson 1981; Dymond et al. 1984; Lei and Boström 1995; Hein and Koschinsky 2012). Interestingly, the change of metal concentration at the onset of the diagenetic transformation is accompanied by a five-fold increase of Mg (0.84 to 4.06 wt. %) and a two-fold decrease of Ca (2.38 to 1.31 wt. %). Because the two alkaline earth divalent cations compensate the layer charge of phyllomanganates (Kuma et al. 1994), Mg is likely exchanged for Ca. However, the exchange is not equimolar; more Mg atoms seem to be introduced than Ca atoms are removed. We will return to this point when discussing the spectroscopic data.

Metal distribution

Micro-SXRF imaging of Mn, Fe, and trace metals confirms the clear chemical distinction of the two general types of nodules (Figs. 5 and 6, Supplementary Fig. 2). Three distinct associations are seen when Ni or Cu is added in red to the bicolor representation of the two elements: green for Fe (gFe) and blue for Mn (bMn). The diagenetic areas appear magenta, the hydrogenetic areas appear violet, and some areas remain green. The green areas also remain unchanged when Ce, Co, or Pb are added in red instead of Ni or Cu. Therefore, the nodule contains two main pools of Fe, one associated with Mn in a Mn/Fe ratio < 2.5 wt. % and with Ce, Co, and Pb, and one without any Mn and poor in trace metals. Accordingly, the Mn-free Fe pool appears black when only Mn is represented on the SXRF map (bMn image of Fig. 5a). The two Fe pools are also distinguished on the correlation graphs between the

Kα(Fe) and Kα(Mn) intensities (Fig. 7). They correspond to the groups of points labeled C (clay) and H (hydrogenetic) in Figure 7. Neither the C nor the H fields shows a correlation between Fe and Mn, which suggests that Fe and Mn are in different mineral species. Although depleted in Fe (Mn/Fe > 2.5), the diagenetic D field shows a negative relationship between Fe and Mn. This observation provides a hint that two Mn phases likely co-exist in diagenetic regions, one associated with Fe similar to the H pool, and another which is Fe-free. We deduce from these observations that Fe and Mn each exists in two distinct mineralogical forms. This inference is confirmed below from the X-ray diffraction and absorption results.

The inverse relationship of Co, Ce, Pb to Ni, Cu as a function of the Mn/Fe ratio observed in Figure 4 by EPMA is neatly demonstrated with bicolor representations. When Ni is green and Co or Pb is red, all colored regions appear monochromatic with no apparent variation in hue (Figs. 5 and Supplementary 2). However, EPMA analysis indicates that the three metals occur everywhere in the Fe-Mn regions. In reality the green and red colors are mixed but secondary hues are faint and cannot been seen by eye alone. A quantitative approach is to calculate correlations of the fluorescence intensities on a pixel-by-pixel basis (Table 1). Calculations show that Ni is moderately anti-correlated with both Pb (r(Ni-Pb) = -0.42 and -0.36 and Co (r(Ni-Co) = -0.37 and -0.42, in agreement with the incomplete separation of metals in the hydrogenetic and diagenetic regions. However, element correlations are misleading in heterogeneous materials that have multiple populations of the same element, each with its own pattern of association. This is the case for Co, which is better correlated to Fe (r(Co-Fe) = 0.77 and 0.54) than to Mn (r(Co-Mn) = -0.16 and -0.44) simply because there are places where Mn is associated with Fe and Co (hydrogenetic regions), and places where Mn occurs alone (diagenetic regions). Early observation of the Co correlation with Fe was interpreted incorrectly to result from the isomorphic substitution of Co^{3+} for Fe^{3+} in ferric oxyhydroxides (Burns and Fuerstenau 1966; Lei and Boström 1995) and from the specific adsorption and oxidation of Co^{2+} to Co^{3+} on siliceous ferric oxyhydroxides particles (Halbach et al. 1982).

Mineralogy

Fe phases. Sixteen μ-XRD patterns and μ-SXRF spectra were recorded at POIs in Fe regions from the three SXRF maps shown in Figures 5 and 6, and Supplementary Figure 2. Iron is essentially present in association with vernadite in the H regions and with dioctahedral smectite in the C (clay) regions (Fig. 8a). Goethite also was detected in some spots. The Fe-vernadite pattern is characterized by broad reflections at 2.455(1) Å (100 reflection) and 1.420(1) Å (110 reflection) from the phyllomanganate component, and two broad reflections at ~2.20 Å and 1.70 Å from the Fe oxyhydroxide component (Varentsov et al. 1991; Manceau et al. 1992, 2007). When observed, the basal reflections at 9.6 Å (001) and 4.8 Å (002) from the vernadite component are faint because the stacking of the Mn layers is disrupted by the epitaxial intergrowth of the Fe nanoparticles (Burns and Burns 1975, 1979; Golden et al. 1988; Manceau and Combes 1988). The composite assemblage has a Kα(Mn)/Kα(Fe) ratio ranging typically from 1.0 to 1.2, consistent with EPMA analysis (Fig. 8b). The nature of the Fe nanophase was further characterized by Fe K-edge EXAFS spectroscopy. The best spectral match to our Fe (oxyhydr)oxide database (Manceau and Drits 1993) was obtained with feroxyhite (δ-FeOOH) (Supplementary Fig. 3). Ferrihydrite, which has a distinct EXAFS signature at k = 5.30 $Å^{-1}$ and 7.60 $Å^{-1}$ (Manceau 2011), is an incompatible model.

In C regions, diffraction maxima and scaterring profiles at 10-13 Å, 4.48 Å, 2.57 Å, 2.40 Å, and 1.50 Å match known 001 and *hk*0 reflections of aluminous dioctahedral smectites (Fig. 8a). In some cases, the 060 reflection is a doublet with one maximum at 1.500 Å and another at 1.514 Å (Supplementary Fig. 4). The 1.514 Å reflection is intermediate between those of aluminous (1.500 Å) and ferric (1.52 Å) smectites, namely montmorillonite/beidellite and nontronite (Brindley and Brown 1980; Badaut et al. 1985; Srodon et al. 2001). Nontronite with *d*(060) spacings of 1.518 Å and 1.521 Å was reported in marine Fe-Mn crusts (Dekov et al. 2011). Because of this previous report of nontronite, and because the intensity of the 1.514 Å reflection varied with the intensity of the Fe(Kα) signal measured simultaneously on the same spots (Vespa et al. 2010), the 1.514 Å reflection is attributed here to dioctahedral (Fe,Al)-smectite. It follows from coupled μ-XRD and μ-SXRF that Fe occurs in smectite as a subsitutional cation and in the precipitates as nanocrystalline feroxyhite. This is the first time that the two Fe forms have been identified in-situ in an intact nodule. Only the second mineral species is potentially metalliferous because μ-SXRF imaging showed that the clay-rich regions have no trace metals.

Mn phases. Micro XRD patterns were collected on 22 diagenetic spots from the three μ-SXRF maps. A clear relationship was observed between the Fe concentration and the XRD trace. The XRD pattern of the high Fe end-member resembles the Fe-vernadite pattern, with a decrease in the feroxyhite component as the Fe content declines. The low Fe end-member is a mixture of 10Å-vernadite and todorokite (Fig. 8a). Todorokite has a prominent diffraction line at 2.40 Å, observed as a second maximum to the right of the 100 reflection from 10Å-vernadite. In addition, todorokite has reflections in the 2.2-1.7 Å interval, which modulate the pattern of vernadite between the 100 and 110 reflections differently from feroxyhite in Fe-vernadite. The increase of todorokite with a decrease of Fe observed at high diffraction angle is accompanied at low angle by the enhancement of the 001 and 002 basal reflections at 9.6-9.7 Å and 4.8 Å (Supplementary Fig. 5). The 7.1 Å (001) and 3.5 Å (002) basal reflections from the one-water (1W) layer hydrated form (7Å-vernadite) are observed in some patterns, but the 2W sets of reflections always prevails.

The reinforcement of the 00*l* reflections with increasing amounts of todorokite probably results from the pillaring with triple octahedral chains of the interlayer space of the phyllomanganate, as reported previously for a deep-sea nodule from a low-temperature hydrothermal field (Fig. 1) (Bodei et al. 2007). The two types of MnO_{2-x} interlayers, those fully hydrated and those whose adjacent layers are bridged with triple chain pillars, can be distinguished by dehydration in vacuum or heating to 80-150 °C, similarly to 2W/1W smectites (Yoshikawa 1991; Ferrage et al. 2005; Manceau et al. 2007). For technical reasons, dehydration could not be performed in-situ during the synchrotron measurements, therefore a fragment of nodule taken from the outer region was dehydrated in vacuum in the laboratory. Several marine Mn oxides, chosen to represent the variety of manganese minerals observed in diagenetic and hydrothermal environments (todorokite, hexagonal birnessite, asbolane), also were analyzed by powder XRD at room condition and in vacuum for comparison and to ascertain that no important Mn phases had been missed (Supplementary Fig. 6). At room condition, the D465 powder appears to be composed of Fe-vernadite and 10Å-vernadite. Todorokite is not detected at high diffraction angle, and only indirectly at low angle from the high intensity of the two basal reflections from 10Å-vernadite. The removal in vacuum of one water layer causes the 10 Å reflection from the 2W

layers to shift to 6.7 Å, and the pillared crystallites to collapse to 8.9 Å, thereby revealing the presence of todorokite. In hydrothermal nodules containing a high proportion of well-crystallized todorokite, the basal reflection decreases less in vacuum, from 9.6-9.7 Å to 9.3-9.4 Å (Supplementary Fig. 6). The greater decrease of 9.6-9.7 Å to 8.9 Å observed in the D465 nodule is related to the incomplete topotactic transformation of 10Å-vernadite to todorokite at the early stage of the diagenetic reaction. Comparison with the mineralogy of hydrothermal nodules shows the absence of hexagonal birnessite, which is a *c*-ordered form of 7Å-vernadite (Drits et al. 1997), and also asbolane, which has a mixed-layer structure (Supplementary Fig. 6) (Manceau et al. 1992).

Fe-vernadite and 10Å-vernadite both have a $d(100)$ / $d(110)$ ratio of 2.455(1) / 1.420(1) ~ $\sqrt{3}$, which indicates that the phyllomanganate layers have hexagonal symmetry with $a = b = 2.84$ Å. This metric parameter needs to be corrected for diffraction effects, which shift the maximum of the two *hk*0 reflections to higher scattering angles (i.e., lower *d* values) for nanosized compared to larger-sized materials (Supplementary Fig. 7) (Manceau et al. 2013). The actual value, obtained by X-ray simulation, is $b = 2.85$ Å. Because Mn^{3+} is larger than Mn^{4+}, the layer dimension can be used to estimate the amount of Mn^{3+} in the MnO_{2-x} octahedral sheets, with the provision that *b* also depends on the density of vacancies. Natural vernadite with no layer Mn^{3+} has an apparent *b* value of 2.83 Å (Manceau et al. 2007), and an actual value of 2.84 Å. Synthetic vernadite (δ-MnO_2) equilibrated at pH 10 has 12% layer Mn^{3+}, 10% vacancies, and a corrected *b* parameter of 2.853 Å (Lanson et al. 2000; Manceau et al. 2013). Synthetic hexagonal birnessite (HBi) equilibrated at pH 4 has 13% Mn^{3+} in its layer, 17% vacancies, and a *b* parameter of 2.848 Å. On the basis of this comparison, the nodule vernadite has about 10-15% layer Mn^{3+}.

The valence states of Mn in Fe-vernadite and 10Å-vernadite were measured by XANES spectroscopy and determined using an extended database of reference spectra (Manceau et al. 2012). The XANES spectra for the two phyllomanganates are compared in Figure 9a. Fe-vernadite has a greater white line corresponding to Mn^{4+}, and 10Å-vernadite a broad shoulder in the rising part of the edge, which is distinctive of Mn^{2+}. Trivalent Mn appears in Mn-XANES spectra as a shoulder below the edge maximum. The rounded maximum of the 10Å-vernadite spectrum is suggestive of a higher proportion of Mn^{3+}. Spectral features are better discerned in the derivative spectra. The derivative of Fe-vernadite closely matches that of the HBi reference, which has the nominal formula $Mn^{3+}_{0.11}Mn^{2+}_{0.055}H^{+}_{0.33}(Mn^{4+}_{0.722}Mn^{3+}_{0.11}W_{0.167})O_2 \cdot 0.5H_2O$ (Lanson et al. 2000) (Fig. 9b). The valence composition of HBi determined previously by XANES is $0.69Mn^{4+} + 0.24Mn^{3+} + 0.07Mn^{2+}$ (average = 3.62) (Manceau et al. 2012). The sensitivity of the XANES derivatives to the Mn valence is shown in Figures 9c and 9d with the hexagonal birnessite reference KBi8 (average = 3.83) and todorokite (average = 3.72). Triclinic birnessite is an incompatible model because it gives a distinct derivative, as shown in Figure 3 of Manceau et al. (2012). The best agreement between 10Å-vernadite and reference spectra was obtained with a biogenic phyllomanganate of valence composition $0.61Mn^{4+} + 0.23Mn^{3+} + 0.16Mn^{2+}$ (Fig. 9e). However, the 10Å-vernadite spectrum has a lower amplitude at 6557 eV (Mn^{4+}) and a higher amplitude at 6547 eV (Mn^{3+}) than the reference, which is indicative of a more reduced state in the sample. Since the 10Å-vernadite spectrum did not match exactly any entry in our spectral library, its valence composition was calculated by least-squares fitting of its spectrum to our complete database under the constraint of non-negativity in the loadings (Combo fit). This approach is more robust than regression analysis with a limited set of model compounds, because irrelevant references,

which give negative loadings, are removed from the fit. The result is $0.39Mn^{4+} + 0.50Mn^{3+} + 0.11Mn^{2+}$ (average = 3.28), in agreement with phenomenological observations (Fig. 9f).

Having shown that Mn had the same average oxidation state in Fe-vernadite and HBi, mineralogical characterization was pursued by comparing its local structure in the two minerals by Mn K-edge EXAFS spectroscopy. Not surprisingly, the two spectra resemble those of phyllomanganates with hexagonal layer structure (Fig. 10a) (Villalobos et al. 2006). The Mn^{3+} and Mn^{4+} cations are not ordered in the MnO_2 layer, as in some bioprecipitated Mn oxides (Webb et al. 2005), otherwise the oscillation at k = 8.1 $Å^{-1}$ would show the double antinode feature observed in triclinic birnessite (Gaillot et al. 2003, 2007; Manceau 2004). Also, it is known that when there is interlayer Mn octahedra that share corners with the layer octahedra, a shoulder appears at k = 6.5 $Å^{-1}$ and a peak in the Fourier transform magnitude at $R + \Delta R$ = 3 Å (Manceau et al. 1997; Silvester et al. 1997; Gaillot et al. 2003). The two structural fingerprints are observed in HBi, which has 17% interlayer Mn, but not in the hydrogenetic nodule (Figs. 10a and 10b). The local structure of Mn in the diagenetic nodule was not examined by this technique because Mn is present in 10Å-vernadite and todorokite.

We conclude from our XRD, Mn-XANES and Mn-EXAFS investigation that the Mn is in the form of a turbostratic phyllomanganate (i.e., vernadite) with no interlayer Mn in the hydrogenetic nodule, and in turbostratic phyllomanganate and todorokite in the diagenetic nodule. The average oxidation state of Mn is 3.62 ± 0.04 v.u. in the first region and 3.28 ± 0.04 v.u. in the second. The fraction of Mn^{3+} to total Mn in Fe-vernadite is estimated to be 10-15% using diffraction (*b* parameter) and 23% using XANES spectroscopy. The difference probably falls within the range of compositional variability of this poorly-ordered and non-stoichiometric nanophase. Diagenetic MnO_2 has more Mn^{3+} in its structure than Fe-vernadite. The higher charge deficit introduced by Mn^{3+}, but also by Ni and Cu (see below), for Mn^{4+} substitution in diagenetic MnO_2 is consistent with the increase of Mg measured by EPMA (Fig. 4).

Crystal chemistry of trace metals

Co and Ni. We examine now how Co and Ni are incorporated in the ferromanganese nodule. One Co-EXAFS spectrum was recorded in the hydrogenetic region and one Ni-EXAFS spectrum in the diagenetic region of Map 1. Measurements were not repeated on different spots because the two spectra appeared to confirm what was largely expected of the structural forms of the two metals; that is, the incorporation of Co as Co^{3+} into the vernadite layer by replacement of Mn, and the partitioning of Ni between vernadite and todorokite (Bodei et al. 2007; Takahashi et al. 2007). The first mechanism is demonstrated in Figure 10c by comparing the hydrogenetic Co-EXAFS spectrum with the spectra of two references, a Co-sorbed birnessite of chemical formula:

$$Mn^{2+}_{0.07}Mn^{3+}_{0.04}Co^{3+}_{0.01}(Mn^{4+}_{0.72}Mn^{3+}_{0.11}Co^{3+}_{0.06}\square_{0.11})O_{1.68}(OH)_{0.32}$$

and CoOOH which has a phyllomanganate-type layered structure (Manceau et al. 1997). The Co-sorbed birnessite reference is the nearest fit for the nodule spectrum. The features in the two spectra are similar, in contrast to those for CoOOH which show a higher amplitude and also a distinct shape at k < 8 $Å^{-1}$. Fourier transforms indicate that Co-sorbed birnessite has a nearest Co-Mn peak at $R+\Delta R$ = 2.4 Å from edge-sharing CoO_6-MnO_6 octahedra in the Mn layer, and a next-nearest Co-Mn peak at $R+\Delta R$ = 3.1 Å from TC-sharing between layer CoO_6 octahedra and interlayer $Mn(O,H_2O)_6$ octahedra (Fig. 3). The second peak (peak C) is absent in the nodule spectrum (Fig. 10d). We interpret this result to

indicate that the vernadite layer has no Mn or Co in its interlayer, consistent with Mn-EXAFS results. The Co in this spot of the sample is structurally incorporated in the natural vernadite, as is consistent with previous findings (Burns 1976; Manceau et al. 1997).

The Ni-EXAFS spectrum, when compared to those of natural and synthetic references (Supplementary Fig. 8), most closely resembles the 50GCC spectrum from hydrothermal Mn deposits in hemipelagic sediments off Costa Rica (Fig. 10e) (Bodei et al. 2007, 2008; Steinmann et al. 2012). High-resolution transmission electron microscopy (HRTEM) coupled with microanalysis showed that 50GCC is a mixture of 10Å-vernadite and todorokite with Ni partitioned almost evenly between the two phases (Bodeï et al. 2007). In todorokite, NiO_6 octahedra located in one tunnel wall are corner-linked to MnO_6 octahedra from the adjacent tunnel wall at a Ni-Mn distance of ~3.50 Å. This distance, which appears on the Fourier transform as a peak at $R + \Delta R$ =3.2 Å similar to the Co-Mn and Mn-Mn TC-linkages described previously, is clearly observed on the diagenetic data (Fig. 10f). Consequently, we conclude that Ni co-exists in 10Å-vernadite and todorokite in marine ferromanganese nodules transformed by early diagenetic reactions. In 10Å-vernadite, Ni is likely totally incorporated in the vacancy sites of the Mn layer, as observed in other natural phyllomanganates (Manceau et al. 2002c; Peacock and Sherman, 2007a).

Cu. Results from Cu-sorbed phyllomanganates show that Cu uptake on the basal surfaces of birnessite and δ-MnO_2 is pH-dependent: it occurs preferentially as a TC complex at acidic pH (peak C at *d*(Cu-Mn)= 3.40 Å), and an E complex at pH circumneutral (peak B at *d*(Cu-Mn)= 2.87 Å) (Fig. 11; Supplementary Fig. 9). The effect of pH on the Cu site occupation is observed regardless of whether or not Cu is added to the birnessite surface at pH ≤ 7, or incorporated initially into the birnessite structure at basic pH (TcBi) and the suspension subsequently equilibrated to lower pH (Table 2; Supplementary Fig. 10). The results are in agreement with previous studies on Cu and Ni sorption on phyllomanganate (Manceau et al. 2007; Peacock and Sherman 2007a, 2007b; Peacock 2009; Sherman and Peacock 2010). However, the Fourier transform of Cu sorbed on δ-MnO_2 at pH 5 (CudBi3-5) shows evidence for a longer Cu-Mn scattering path at R = 3.68 Å not described previously, which is the distance expected for Cu sorbing to the edge sites via a bidentate corner-sharing linkage (DC complex) (Fig. 3) (Manceau et al. 2007). An inspection of all data reveals that this contribution is always present, but its contribution to the EXAFS signal is negligible in HBi because the fractional amount of the layer-edge complex is low because of the large layer dimension. Thus, peak C in reality is a doublet made of the TC and DC complexes, which is only resolvable when the sorbent surface has a smaller fraction of vacancy sites (TC complex) relative to edge sites (DC complex) available for surface complexation.

Three micro Cu-EXAFS spectra were recorded on the nodule thin section: one in regions rich in smectite (Map 1), one in a diagenetic vein rich in 10Å-vernadite and poor in todorokite as indicated by μ-XRD (Map 2), and one on concentrated Cu areas from diagenetic regions containing high amounts of todorokite (Map 1). From the comparison of the three EXAFS spectra shown in Figure 12a, it is clear that Cu is bound differently in the three regions. The EXAFS collected in the organo-clay matrix is featureless with the signal made of only one electronic wave from the Cu-O coordination shell. The two other spectra show a second wave oscillation at k = 5.5 $Å^{-1}$, which occurs when there is a metal shell beyond the oxygen shell. The Fourier transform of the first spectrum confirms that the local order is limited to the nearest-neighbor shell of oxygen, which we attribute to disorder arising from the

multiplicity of the binding Cu environments (Fig. 12b). Ferromanganese nodules from abyssal plains typically contain organic matter and biogenic silica, phosphates, and carbonates (Peacock and Sherman 2007a; Hein et al. 2012), which may take up Cu (and also Ni) in addition to aluminosilicates and Fe-Mn oxides (Boström and Nayudu 1974; Boström et al. 1974). The Fourier transform for 10Å-vernadite shows evidence for a Cu-Mn scattering best modeled with 1.6 Mn at 2.88 Å (Supplementary Fig. 10). Copper has become structurally incorporated into the MnO_2 layer by occupying some vacancy sites. However, the low number of Mn neighbors, which nominally should be six if all the Cu were in the MnO_2 layer, suggests that the diagenetic vein has an abundant hydrogenetic component. In the highly diagenetically transformed region of the nodule, a second Mn shell at a distance characteristic of corner-sharing linkage (peak C) is detected. Because the analyzed spots have high amounts of todorokite, the likely origin of this feature is the incorporation of Cu into todorokite, similarly to Ni.

Chemical formulae and metal uptake capacity of todorokites

Because todorokite is the stable phase and its amount is correlated positively with the Mn/Fe ratio, an average chemical formula can be calculated from the three nodule spots with the highest value of the Mn/Fe ratio (> 100), as measured by electron microprobe analysis (Fig. 4, Supplementary Table S1). The three point formulae obtained by balancing the charges on the cations in the framework sites (in parentheses) and tunnel sites are:

Mn/Fe (wt%) =216.50 $Mg^{2+}_{0.222}Ca^{2+}_{0.041}K^{+}_{0.018}Na^{+}_{0.007}(Mn^{4+}_{0.569}Mn^{3+}_{0.310}Co^{3+}_{0.001}Ni^{2+}_{0.078}Cu^{2+}_{0.043})O_2 \cdot nH_2O$

Mn/Fe (wt%) =160.86 $Mg^{2+}_{0.204}Ca^{2+}_{0.046}K^{+}_{0.026}Na^{+}_{0.016}(Mn^{4+}_{0.568}Mn^{3+}_{0.321}Co^{3+}_{0.003}Ni^{2+}_{0.067}Cu^{2+}_{0.042})O_2 \cdot nH_2O$

Mn/Fe (wt%) =102.00 $Mg^{2+}_{0.199}Ca^{2+}_{0.042}K^{+}_{0.023}Na^{+}_{0.012}(Mn^{4+}_{0.602}Mn^{3+}_{0.278}Co^{3+}_{0.002}Ni^{2+}_{0.082}Cu^{2+}_{0.036})O_2 \cdot nH_2O$

which average to:

$$Mg^{2+}_{0.208}Ca^{2+}_{0.043}K^{+}_{0.022}Na^{+}_{0.012}(Mn^{4+}_{0.580}Mn^{3+}_{0.303}Co^{3+}_{0.002}Ni^{2+}_{0.076}Cu^{2+}_{0.040})O_2 \cdot nH_2O.$$

Based on the crystal structure of todorokite, the cations in the tunnel interior cannot exceed a total of 1.0 cation per unit cell, which corresponds to a ratio of tunnel to framework cations of 1/6 (Post and Bish 1988; Lei 1996). Two chemical formulae have been proposed for terrestrial todorokites, one by Gutzmer and Beukes (2000):

$$Mg^{2+}_{0.07}Ca^{2+}_{0.03}Na^{+}_{0.06}K^{+}_{0.01}(Mn^{4+}_{0.80}Mn^{3+}_{0.17}W_{0.02}Fe^{3+}_{0.01}Al^{3+}_{0.01})O_2 \cdot 0.55H_2O$$

and another by Post et al. (2003)

$$Mg^{2+}_{0.07}Ca^{2+}_{0.02}Na^{+}_{0.07}(Mn^{4+}_{0.73}Mn^{3+}_{0.27})O_2 \cdot 0.7H_2O.$$

In both cases, the amount of tunnel cations is equal to the number of tunnel sites available per formula unit ($0.16 \approx 1/6$). The excess of tunnel cations in our calculated formula ((0.208+0.043+0.022+0.012) - 1/6 = 0.12) can be explained by the common association of todorokite with the authigenic zeolite phillipsite in marine nodules (Burns and Burns 1978a; Lee and Lee 1998; Bodei et al. 2007). Lee and Lee (1998) proposed the following formula for phillipsite in manganese nodules of the northeastern equatorial Pacific basin: $Mg^{2+}_{0.3}Ca^{2+}_{0.1}Na^{+}_{1.1}K^{+}_{1.5}(Fe_{0.3}Al_{4.2}Si_{11.8})O_{32} \cdot 10H_2O$. Assuming that Na, K, Ca and the excess Mg are in phillipsite and other mineral impurities, the chemical formula for the nodule todorokite studied here can be recalculated as:

$$Mg^{2+}_{0.167}(Mn^{4+}_{0.783}Mn^{3+}_{0.099}Co^{3+}_{0.002}Ni^{2+}_{0.076}Cu^{2+}_{0.040})O_2 \cdot nH_2O.$$

The proposed formula is supported by the inter-element relationship in Figure 4c, which shows that Na has no, K little, and Ca a negative correlation with the Mn/Fe ratio; hence are not associated with todorokite. By analogy with the nodule todorokite, the hydrothermal marine todorokite studied by Bodei et al. (2007) also can be considered to be saturated by Mg. Accordingly, its formula proposed originally

$$Mg^{2+}_{0.178}Ca^{2+}_{0.013}K^{+}_{0.019}(Mn^{4+}_{0.612}Mn^{3+}_{0.356}Ni^{2+}_{0.032})O_2 \cdot nH_2O$$

can be recalculated as:

$$Mg^{2+}_{0.167}(Mn^{4+}_{0.699}Mn^{3+}_{0.269}Ni^{2+}_{0.032})O_2 \cdot nH_2O\,.$$

The nodule todorokite is strongly enriched in Ni and Cu and has a (Ni+Cu+Co)/Mn ratio of 0.13, which is slightly lower than the ~0.167 (or about 1/6) upper limit suggested by Usui (1979) from bulk nodule analyses. The highest metal uptake capacity is reached when the 0.167 tunnel sites are all occupied by a divalent cation (mostly Mg^{2+}) and when the low-valence octahedral cations that balance the intratunnel charge of +0.33e are all Ni^{2+} and Cu^{2+} cations, without Mn^{3+}. Lastly, it is worthwhile comparing the cationic composition of the todorokite framework ($Mn^{4+}_{0.783}Mn^{3+}_{0.099}Co^{3+}_{0.002}Ni^{2+}_{0.076}Cu^{2+}_{0.040}$) to the Mn valence composition of 10Å-vernadite ($Mn^{4+}_{0.61}Mn^{3+}_{0.23}Mn^{2+}_{0.16}$). One notes that [$Mn^{3+}$] in 10Å-vernadite ≈ ∑([$Mn^{3+}$] + [$Co^{3+}$] + [$Ni^{2+}$] + [$Cu^{2+}$]) in todorokite, which supports the view that these other metals substitute for Mn^{3+} in the edge sites of the todorokite framework (Fig. 1) (Burns and Burns 1985; Post et al. 2003).

IMPLICATIONS

To date, there is a regain of interest in mining marine metal deposits (Co, Ni, Cu, Li, Mo, REEs…) in order to augment the production from land-based deposits (Hein et al 2013). A good understanding of the forms and enrichment mechanisms of these elements in crust-nodule ferromanganese deposits is a necessary prerequisite for the effective mining and optimal processing of this resource. The present study shows how the mineralogy of polymetallic nodules on sediment-covered abyssal plains controls the concentration of metals and how the mineralogy is modified diagenetically by geochemical reactions that occur in suboxic conditions at the sediment-water interface.

We showed that metallifeous 10Å-vernadite in diagenetic veins of the hydrogenetic nodule is composed of non-collapsable and collapsable (to 7 Å) vernadite crystallites, which we interpret to indicate that the first have Mg^{2+} and todorokite pillars in the interlayer, whereas the second have none of those (Sun et al. 2012). The 10Å-vernadite also has better crystallinity and more reduced Mn cations (Mn^{2+} and Mn^{3+}) than the adjacent Fe-vernadite in the unaltered hydrogenetic nodule, which indicates that 10Å-vernadite precipitated directly from solution. The as-formed 10Å-vernadite is metastable and is eventually replaced by todorokite via topotactic transformation.

Our results do not confirm the suggested existence in authigenic 10Å-vernadite of "buserite-II" phyllomanganate layers, which are characterized by a high proportion of Mn (and possibly other transition metals) as interlayer cation (Fig. 2) (Novikov and Bogdanova 2007 ; Pal'chik et al. 2011). The absence (or scarcity) of interlayer Mn in unpillared vernadite is consistent with the pH-dependence of the δ-MnO_2 structure, which shows that the proportion of interlayer Mn is low at the seawater pH of ~8 and high at acidic pH (Manceau et al. 2013). Neither orderly stacked birnessite (7Å-manganate) nor

asbolane-type mix-layers (10Å-manganate), which occur in hydrothermal deposits (Supplementary Fig. 6), were identified.

Here, we also documented for the first time the diversity of the Cu coordination environments in manganese nodules. In the organo-clay matrix, Cu appears to be bound in several forms, as indicated by the lack of Cu-metal signal by EXAFS. This pool likely includes organically complexed Cu which eventually becomes available for uptake in authigenic 10Å-vernadite and todorokite during dissimilatory bio-oxidation of organic material and concomitant reduction of hydrogenetic vernadite (Burns and Burns 1978b; Lovley and Philips 1988). The incorporation of Cu^{2+} in Mn^{3+}-containing 10Å-vernadite and todorokite is favored by the Jahn-Teller distortion of the $[CuO]_6$ coordination environment. Finally, the Co, Ni, and Cu K-edge EXAFS spectra are provided as supplementary material to facilitate further identification of metal coordination environments in Mn oxides.

ACKNOWLEDGMENTS

Samples D465, D11-X9, and D12-X2 were provided by Dr. A. Usui. The Advanced Light Source is supported by the Director, Office of Science, Office of Basic Energy Sciences, of the U.S. Department of Energy under Contract No. DE-AC02-05CH11231.

SUPPLEMENTARY MATERIALS

[1] Deposit item **XX**, Supplementary tables and figures in PDF, complete EPMA analyses in Excel format, and one ASCII file (Co-, Ni-, and Cu-XAS data).

REFERENCES CITED

Arrhenius, G., and Tsai, A. (1981) Structure, phase transformation and prebiotic catalysis in marine manganate minerals. (SIO Ref. Ser., 81-28). Scripps Institution of Oceanography, La Jolla, CA.

Badaut, D., Besson, G., Decarreau, A., and Rautureau, R. (1985) Occurrence of a ferrous trioctahedral smectite in recent sediments of Atlantis II Deep, Red Sea. Clay Minerals, 20, 389-404.

Bilinski, H., Giovanoli, R., Usui, A., and Hanzel, D. (2002) Characterization of Mn oxides in cemented streambed crusts from Pinal Creek, Arizona, USA, and in hot-spring deposits from Yuno-Taki falls, Hokkaido, Japan. American Mineralogist, 87, 580-591.

Bodei, S., Buatier, M., Steinmann, M., Adatte, T., and Wheat, C.G. (2008) Characterization of metalliferous sediment from a low-temperature hydrothermal environment on the Eastern Flank of the East Pacific Rise. Marine Geology, 250, 128-141.

Bodei, S., Manceau, A., Geoffroy, N., Baronnet, A., and Buatier, M. (2007) Formation of todorokite from vernadite in Ni-rich hemipelagic sediments. Geochimica et Cosmochimica Acta, 71, 5698–5716.

Boström, K., Joensuu, O., and Brohm, I. (1974) Plankton: its chemical composition and its significance as a source of pelagic sediments. Chemical Geology, 14, 255-271.

Boström, K., and Nayudu, Y.R. (1974) The origin of manganese nodules on the ocean floor. American Journal of Science, 263, 17-39.

Brindley, G.W., and Brown, G. (1980) *Crystal structures of clay minerals and their X-ray identification*. 495 p. Mineralogical Society, London.

Buatier, M.D., Guillaume, D., Wheat, C.G., Hervé, L., and Adatte, T. (2004) Mineralogical characterization and genesis of hydrothermal Mn oxides from the flank of the Juan the Fuca Ridge. American Mineralogist, 89, 1807-1815.

Burns, R.G. (1976) The uptake of cobalt into ferromanganese nodules, soils, and synthetic manganese (IV) oxides. Geochimica et Cosmochimica Acta, 40, 95-102.

Burns, R.G., and Burns, V.M. (1975) Mechanism for nucleation and growth of manganese nodules. Nature, 255, 130-131.

-. (1979) Manganese oxides. In R.G. Burns, Ed. Marine Minerals, vol. 6, p. 1-46. Mineralogical Society of America.

Burns, R.G., Burns, V.M., and Stockman, H.W. (1983) A review of the todorokite-buserite problem: implications to the mineralogy of marine manganese nodules. American Mineralogist, 68, 972-980.

-. (1985) The todorokite-buserite problem: further considerations. American Mineralogist, 70, 205-208.

Burns, R.G., and Fuerstenau, D.W. (1966) Electron-probe determination of inter-element relationships in manganese nodules. American Mineralogist, 51, 895-902.

Burns, V.M., and Burns, R.G. (1978a) Authigenic todorokite and phillipsite inside deep-sea manganese nodules. American Mineralogist, 63, 827-831.

-. (1978b) Post-depositional metal enrichment processes inside manganese nodules from the north equatorial Pacific. Earth and Planetary Science Letters, 39, 341–348.

Calvert, S.E., and Price, N.B. (1977) Shallow water, continental margin and lacustrine nodules: distribution and geochemistry. In G.P. Glasby, Ed. Marine manganese deposits, p. 45-86. Elsevier Oceanography Series.

Chukhrov, F.V., Drits, V.A., Gorshkov, A.I., Sakharov, B.A., and Dikov, Y.P. (1987) Structural models for vernadite. International Geology Review, 29, 1337-1347.

Chukhrov, F.V., Gorshkov, A., Sivtsov, A.V., and Berezovskaya, V.V. (1979) New data on natural todorokites. Nature, 278, 631-632.

Chukhrov, F.V., Gorshkov, A.I., Drits, V.A., and Dikov, Y.P. (1985) Structural varieties of todorokite. International Geological Review, 27, 1481–1491.

Chukhrov, F.V., Gorshkov, A.I., Drits, V.A., Shterenberg, A.V., and Sakharov, B.A. (1983) Mixed-layer asbolan-buserite minerals and asbolans in oceanic iron-manganese concretions. International Geology Review, 25, 838-847.

Chukhrov, F.V., Gorshkov, A.I., Vitovskaya, I.V., Drits, V.A., Sivtsov, A.I., and Rudnitskaya, E.S. (1982) Crystallochemical nature of Co-Ni asbolan. International Geological Review, 24, 598-604.

Chukhrov, F.V., Gorshkov, A.I., Vitovskaya, I.V., Drits, V.A., Sivtsov, A.V., and Rudnitskaya, E.S. (1980) Crystallochemical nature of Co-Ni asbolan. Izvestia Akademia Nauk, SSSR, Seriya Geologicheskaya, 6, 73-81. (Translated in International Geological Review 24, 598-604, 1982).

Cui, H., Liu, X., Tan, W., Feng, X., Liu, F., and Ruan, H.D. (2008) Influence of Mn(III) availability on the phase transformation from layered buserite to tunnel-structured todorokite. Clays and Clay Minerals, 56, 397-403.

Cui, H.J., Feng, X.H., He, J.Z., Tan, W.F., and Liu, F. (2006) Effects of reaction conditions on the formation of todorokite at atmospheric pressure. Clays and Clay Minerals, 54, 605-615.

Cui, H.J., Feng, X.H., Tan, W.F., Zhao, W., Wang, M.K., Tsao, T.M., and Liu, F. (2010) Synthesis of a nanoflbrous manganese oxide octahedral molecular sieve with $Co(NH_3)_6^{3+}$ complex ions as a template via a reflux method. Crystal Growth & Design, 10, 3355-3362.

Davison, W. (1993) Iron and manganese in lakes. Earth-Science Reviews, 34, 119-163.

Dekov, V., Boycheva, T., Halenius, U., Billström, K., Kamenov, G.D., Shanks, W.C., and Stummeyer, J. (2011) Mineralogical and geochemical evidence for hydrothermal activity at the west wall of 12°50′N core complex (Mid-Atlantic ridge): A new ultramafic-hosted seafloor hydrothermal deposit? Marine Geology, 288, 90-102.

Drits, V.A., Silvester, E., Gorshkov, A.I., and Manceau, A. (1997) The structure of synthetic monoclinic Na-rich birnessite and hexagonal birnessite. Part 1. Results from X-ray diffraction and selected area electron diffraction. American Mineralogist, 82, 946-961.

Dymond, J., Lyle, B., Finney, B., Piper, D.Z., Murphy, K., Conard, R., and Pisias, N. (1984) Ferromanganese nodules from MANOP Sites H, S, and R - control of mineralogical and chemical composition by multiple accretionary processes. Geochimica et Cosmochimica Acta, 48, 931-949.

Feng, X.H., Tan, W.F., Liu, F., Wang, J.B., and Ruan, H.D. (2004) Synthesis of todorokite at atmospheric pressure. Chemistry of Materials, 16, 4330-4336.

Ferrage, E., Lanson, B., Sakharov, B.A., and Drits, V.A. (2005) Investigation of smectite hydration properties by modeling experimental X-ray diffraction patterns: Part I. Montmorillonite hydration properties. American Mineralogist, 90, 1358.1374.

Gaillot, A.C., Drits, V.A., Manceau, A., and Lanson, B. (2007) Structure of the synthetic K-rich phyllomanganate birnessite obtained by high-temperature decomposition of $KMnO_4$: Substructures of K-rich birnessite from 1000°C experiment. Microporous and Mesoporous Materials, 98, 267–282.

Gaillot, A.C., Flot, D., Drits, V.A., Burghammer, M., Manceau, A., and Lanson, B. (2003) Structure of synthetic K-rich birnessites obtained by high-temperature decomposition of $KMnO_4$. I. Two-layer polytype from a 800°C experiment. Chemistry of Materials, 15, 4666-4678.

Giovanoli, R. (1980) Vernadite is random-stacked birnessite. Mineralium Deposita, 15, 251-253.

Giovanoli, R., Bürki, P., Giuffredi, S., and Stumm, W. (1975) Layer structured manganese oxide hydroxides. IV: The buserite groups; structure stabilization of transition elements. Chimia, 29, 517-520.

Giovanoli, R., Stähli, E., and Feitknecht, W. (1970) Über oxidhydroxide des vierwertigen mangans mit schichtengitter. 1. Natrium mangan(II,III)- manganat(IV). Helvetica Chimica Acta, 53, 209-220.

Goldberg, E.D. (1954) Marine Geochemistry. 1. Chemical scavengers of the sea. Journal of Geology, 62, 249-265.

Golden, D.C., Chen, C.C., and Dixon, J.B. (1986) Synthesis of todorokite. Science, 231, 717-719.

Golden, D.C., Chen, C.C., Dixon, J.B., and Tokashki, Y. (1988) Pseudomorphic replacement of manganese oxides by iron oxide minerals. Geoderma, 42, 199-211.

Grangeon, S., Lanson, B., Miyata, N., Tani, Y., and Manceau, A. (2010) Structure of nanocrystalline phyllomanganates produced by freshwater fungi. American Mineralogist, 95, 1608-1616.

Grangeon, S., Manceau, A., Guilhermet, J., Gaillot, A.C., Lanson, M., and Lanson, L. (2012) Zn sorption modifies dynamically the layer and interlayer structure of vernadite. Geochimica et Cosmochimica Acta, 85, 302-313.

Gutzmer, J., and Beukes, N.J. (2000) Asbestiform manjiroite and todorokite from the Kalahari manganese field, South Africa. South African Journal of Geology, 103, 163–174.

Halbach, P., Giovanoli, R., and von Borstel, D. (1982) Geochemical processes controlling the relationship between Co, Mn, and Fe in early diagenetic deep-sea nodules. Earth and Planetary Science Letters, 60, 226-236.

Halbach, P., Scherhag, C., Hebisch, U., and Marchig, V. (1981) Geochemical and mineralogical control of different genetic types of deep-sea nodules from the Pacific Ocean. Mineralium Deposita, 16, 59-64.

Hammersley, A.P., Svensson, S.O., Han, M., Fitch, A.N., and Hausermann, D. (1996) Two-dimensional detector software: from real detector to idealised image or two-theta scan. High Pressure Research, 14, 235-248.

Hein, J.R., Conrad, T.A., Frank, M., Christl, M., and Sager, W.W. (2012) Copper-nickel-rich, amalgamated ferromanganese crust-nodule deposits from Shatsky Rise, NW Pacific. Geochemistry Geophysics Geosystems, 13, Q10022.

Hein, J.R., and Koschinsky, A. (2012) Deep-ocean ferromanganese crusts and nodules. Elsevier, New York.

Hein, J.R., Mizell, K., Koschinsky, A., and Conrad, T.A. (2013) Deep-ocean mineral deposits as a source of critical metals for high- and green-technology applications: Comparison with land-based resources. Ore Geology Reviews, 51, 1-14.

Hlawatsch, S., Kersten, M., Garbe-Schönberg, C.D., Lechtenberg, F., Manceau, A., Tamura, N., Kulik, D.A., Harff, J., and Suess, E. (2001) Trace metal fluxes to ferromanganese nodules from the western Baltic Sea as a record for long-term environmental changes. Chemical Geology, 182, 697-710.

Hlawatsch, S., Neumann, T., van den Berg, C.M.G., Kersten, M., Harff, J., and Suess, E. (2002) Fast-growing, shallow-water ferro-manganese nodules from the western Baltic Sea: origin and modes of trace element incorporation. Marine Geology, 182, 373-387.

Ito, T., Usui, A., Kajiwara, Y., and Nakano, T. (1998) Strontium isotopic compositions and paleoceanographic implication of fossil manganese nodules in DSDP/ODP cores, Leg 1-126. Geochimica et Cosmochimica Acta, 62, 1545-1554.

Jiang, X.J., Lin, X.H., Yao, D., Zhai, S.K., and Guo, W.D. (2007) Geochemistry of lithium in marine ferromanganese oxide deposits. Deep-Sea Research Part I-Oceanographic Research Papers, 54, 85-98.

Johnson, E.A., and Post, J.E. (2006) Water in the interlayer region of birnessite: Importance in cation exchange and structural stability. American Mineralogist, 91, 609-618.

Kuma, K., Usui, A., Paplawsky, W., Gedulin, B., and Arrhenius, G. (1994) Crystal structures of synlhetic 7 A and 10 Å manganates substituted by mono- and divalent cations. Mineralogical Magazine, 58, 425-447.

Lanson, B., Drits, V.A., Feng, Q., and Manceau, A. (2002a) Crystal structure determination of synthetic Na-rich birnessite: Evidence for a triclinic one-layer cell. American Mineralogist, 87, 1662-1671.

Lanson, B., Drits, V.A., Gaillot, A.C., Silvester, E., Plançon, A., and Manceau, A. (2002b) Structure of heavy metal sorbed birnessite. Part I. Results from X-ray diffraction. American Mineralogist, 87, 1631-1645.

Lanson, B., Drits, V.A., Silvester, E.J., and Manceau, A. (2000) Structure of H-exchanged hexagonal birnessite and its mechanism of formation from Na-rich monoclinic buserite at low pH: New data from X-ray diffraction. American Mineralogist, 85, 826-835.

Lei, C.H. and Lee, S.R. (1998) Authigenic phillipsite in deep-sea manganese nodules from the Clarion-Clipperton area, NE equatorial Pacific. Marine Geology, 148, 125-133.

Lei, G., and Boström, K. (1995) Mineralogical control on transition metal distributions in marine manganese nodules. Marine Geology, 123, 253-261.

Lei, G.B. (1996) Crystal structures and metal uptake capacity of 10 angstrom-manganates: An overview. Marine Geology, 133, 103-112.

Lovley, D.R., and Philips, E.J.P. (1988) Novel mode of microbial energy-metabolism - organic-carbon oxidation coupled to dissimilatory reduction of iron and manganese. Applied and Environmental Microbiology, 54, 1472-1480.

Lynn, D.C., and Bonatti, E. (1965) Mobility of manganese in the diagenesis of deep-sea sediments. Marine Geology, 3, 457-474.

Manceau, A. (2011) Critical evaluation of the revised akdalaite-model for ferrihydrite. American Mineralogist, 96, 521-533.

Manceau, A., and Combes, J.M. (1988) Structure of Mn and Fe oxides and oxyhydroxides: a topological approach by EXAFS. Physics and Chemistry of Minerals, 15, 283-295.

Manceau, A., and Drits, V.A. (1993) Local structure of ferrihydrite and feroxyhite by EXAFS spectroscopy. Clay Minerals, 28, 165-184.

Manceau, A., Drits, V.A., Silvester, E., Bartoli, C., and Lanson, B. (1997) Structural mechanism of Co(II) oxidation by the phyllomanganate, Na-buserite. American Mineralogist, 82, 1150-1175.

Manceau, A., Gorshkov, A.I., and Drits, V.A. (1992) Structural chemistry of Mn, Fe, Co, and Ni in Mn hydrous oxides. II. Information from EXAFS spectroscopy, electron and X-ray diffraction. American Mineralogist, 77, 1144-1157.

Manceau, A., Lanson, B., and Drits, V.A. (2002a) Structure of heavy metal sorbed birnessite. Part III. Results from powder and polarized extended X-ray absorption fine structure spectroscopy. Geochimica et Cosmochimica Acta, 66, 2639-2663.

Manceau, A., Lanson, M., and Geoffroy, N. (2007) Natural speciation of Ni, Zn, Ba and As in ferromanganese coatings on quartz using X-ray fluorescence, absorption, and diffraction. Geochimica et Cosmochimica Acta, 71, 95-128.

Manceau, A., Marcus, M.A., and Grangeon, S. (2012) Determination of Mn valence states in mixed-valent manganates by XANES spectroscopy. American Mineralogist, 97, 816-827.

Manceau, A., Marcus, M.A., Grangeon, S., Lanson, M., Lanson, B., Gaillot, A.C., Skanthakumar, S., and Soderholm, L. (2013) Short-range and long-range order of phyllomanganate nanoparticles

determined using high energy X-ray scattering. Journal of Applied Crystallography, 46, 193-209.

Manceau, A., Marcus, M.A., and Tamura, N. (2002b) Quantitative speciation of heavy metals in soils and sediments by synchrotron X-ray techniques. In P.A. Fenter, M.L. Rivers, N.C. Sturchio, and S.R. Sutton, Eds. Applications of Synchrotron Radiation in Low-Temperature Geochemistry and Environmental Science, 49, p. 341-428. Mineralogical Society of America, Washington, DC.

Manceau, A., Tamura, N., Marcus, M.A., MacDowell, A.A., Celestre, R.S., Sublett, R.E., Sposito, G., and Padmore, H.A. (2002c) Deciphering Ni sequestration in soil ferromanganese nodules by combining X-ray fluorescence, absorption and diffraction at micrometer scales of resolution. American Mineralogist, 87, 1494-1499.

Manceau, A., Marcus, M.A., Tamura, N., Proux, O., Geoffroy, N., and Lanson, B. (2004) Natural speciation of Zn at the micrometer scal in a clayey soil using X-ray ß uorescence, absorption, and diffraction. Geochimica et Cosmochimica Acta, 68, 2467−2483.

Manceau, A., Tommaseo, C., Rihs, S., Geoffroy, N., Chateigner, D., Schlegel, M., Tisserand, D., Marcus, M.A., Tamura, N., and Chen, Z.S. (2005) Natural speciation of Mn, Ni and Zn at the micrometer scale in a clayey paddy soil using X-ray fluorescence, absorption, and diffraction. Geochimica et Cosmochimica Acta, 69, 4007-4034.

Marchig, V., and Gundlach, H. (1981) Separation of iron from manganese and growth of manganese nodules as a consequence of diagenetic ageing of radiolarians. Marine Geology, 40, M35-M43.

Marcus, M.A., MacDowell, A.A., Celestre, R., Manceau, A., Miller, T., Padmore, H.A., and Sublett, R.E. (2004) Beamline 10.3.2 at ALS: a hard X-ray microprobe for environmental and materials sciences. Journal of Synchrotron Radiation, 11, 239-247.

Margolis, S.V., and Glasby, G.P. (1973) Microlaminations in marine manganese nodules as revealed by scanning microscopy. Geological Society of America Bulletin, 84, 3601-3610.

Martin-Barajas, A., Lallier-Verges, E., and Leclaire, L. (1991) Characteristics of manganese nodules from the Central Indian Basin: Relationship with the sedimentary environment. Marine Geology, 101, 249-265.

Mellin, T., and Lei, G. (1993) Stabilization of 10Å-manganates by interlayer cations and hydrothermal treatment: Implications for the mineralogy of marine manganese concretions. Marine Geololgy, 115, 67-83.

Moore, W.S. (1981) Iron-manganese banding in Oneida Lake ferromanganese nodules. Nature, 292, 233-235.

Novikov, G.V., and Bogdanova, O.Y. (2007) Transformations of ore minerals in genetically different oceanic ferromanganese rocks. Lithology and Mineral Resources, 42, 303-317.

Pal'chik, N.A., Grigor'eva, T.N., and Moroz, T.N. (2011) Natural and synthetic manganese minerals. Russian Journal of Inorganic Chemistry, 58, 138-143.

Paterson, E., Bunch, J.L., and Clark, D.R. (1986) Cation exchange in synthetic manganates: I. Alkylammonium exchange in a synthetic phyllomanganate. Clay Minerals, 21, 949-955.

Peacock, C.L. (2009) Physiochemical controls on the crystal-chemistry of Ni in birnessite: Genetic implications for ferromanganese precipitates. Geochimica et Cosmochimica Acta, 73, 3568-3578.

Peacock, C.L., and Sherman, D.M. (2007a) Crystal-chemistry of Ni in marine ferromanganese crusts and nodules. American Mineralogist, 92, 1087-1092.

Peacock, C.L., and Sherman, D.M. (2007b) Sorption of Ni by birnessite: Equilibrium controls on Ni in seawater. Chemical Geology, 238, 94-106.

Piper, D.Z., and Williamson, M.E. (1981) Mineralogy and composition of concentric layers within a manganese nodule from the North Pacific Ocean. Marine Geology, 40, 255-268.

Post, J.E., and Bish, D.L. (1988) Rietveld refinement of the todorokite structure. American Mineralogist, 73, 861–869.

Post, J.E., Heaney, P.J., and Hanson, J. (2003) Synchrotron X-ray diffraction of the structure and dehydration behavior of todorokite. American Mineralogist, 88, 142-150.

Post, J.E., and Veblen, D.R. (1990) Crystal structure determinations of synthetic sodium, magnesium, and potassium birnessite using TEM and the Rietveld method. American Mineralogist, 75, 477-489.

Price, N.B., and Calvert, S.E. (1970) Compositional variation in Pacific Ocean ferromanganese nodules and its relationships to sediment accumulation. Marine Geology, 9, 145-171.

Sherman, D.M., and Peacock, C.L. (2010) Surface complexation of Cu on birnessite (d-MnO_2): Controls on Cu in the deep ocean. Geochimica et Cosmochimica Acta, 74, 6721-6730.

Siegel, M.D., and Turner, S. (1983) Crystalline todorokite associated with biogenic debris in manganese nodules. Science, 219, 172-174.

Silvester, E., Manceau, A., and Drits, V.A. (1997) The structure of synthetic monoclinic Na-rich birnessite and hexagonal birnessite. Part 2. Results from chemical studies and EXAFS spectroscopy. American Mineralogist, 82, 962-978.

Srodon, J., Drits, V.A., McCarty, D.K., Hsieh, J.C.C., and Eberl, D.D. (2001) Quantitative X-ray diffraction analysis of clay-bearing rocks from random preparations. Clays and Clay Minerals, 49, 514-528.

Steinmann, M., Bodei, S., and Buatier, M. (2012) Nd–Sr isotope and REY geochemistry of metalliferous sediments in a low-temperature off-axis hydrothermal environment (Costa Rica margin). Marine Geology, 315, 132-142.

Sun, Z.J., Shu, D., Chen, H., He, C., Tang, S., and Zhang, J. (2012) Microstructure and supercapacitive properties of buserite-type manganese oxide with a large basal spacing. Journal of Power Sources, 216, 425-433.

Takahashi, Y., Manceau, A., Geoffroy, N., Marcus, M.A., and Usui, A. (2007) Chemical and structural control of the partitioning of Co, Ce, and Pb in marine ferromanganese oxides. Geochimica et Cosmochimica Acta, 71, 984-1008.

Takahashi, Y., Shimizu, H., Usui, A., Kagi, H., and Nomura, M. (2000) Direct observation of tetravalent cerium in ferromanganese nodules and crusts by X-ray-absorption near-edge structure (XANES). Geochimica et Cosmochimica Acta, 64, 2929-2935.

Tazaki, K. (2000) Formation of banded iron-manganese structures by natural microbial communities. Clays and Clay Minerals, 48, 511-520.

Tournassat, C., Charlet, L., Bosbach, D., and Manceau, A. (2002) Arsenic(III) oxidation by birnessite and precipitation of manganese(II) arsenate. Environmental Science and Technology, 36, 493-500.

Turner, S., and Buseck, P.R. (1979) Manganese oxide tunnel structures and their intergrowths. Science, 203, 456-458.

-. (1981) Todorokites: a new family of naturally occurring manganese oxides. Science, 1024-1027.

Turner, S., Siegel, M.D., and Buseck, P.R. (1982) Structural features of todorokite intergrowths in manganese nodules. Nature, 296, 841-842.

Usui, A. (1979) Nickel and copper accumulations as essential elements in 10-Å manganite of deep-sea manganese nodules. Nature, 279, 411-413.

Usui, A., Mellin, T.A., Nohara, M., and Yuasa, M. (1989) Structural stability of marine 10A manganates from the Ogasawara (Bonin) arc: Implication for low-temperature hydrothermal activity. Marine Geology, 86, 41-56.

Usui, A., and Mita, N. (1995) Geochemistry and mineralogy of a modern buserite deposit from a hot spring in hokkaido, Japan. Clays and Clay Minerals, 43, 116-127.

Usui, A., Yuasa, M., Yokota, S., Nohara, M., Nishimura, A., and Murakami, F. (1986) Submarine hydrothermal manganese deposits from the Ogasawara (Bonin) Arc, off the Japan Islands. Marine Geology, 73, 311-322.

Varentsov, I.M., Drits, V.A., Gorshkov, A.I., Sivtsov, A.V., and Sakharov, B.A. (1991) Me-Fe oxyhydroxide crusts from Krylov Seamount (Eastern Atlantic): Mineralogy, geochemistry and genesis. Marine Geology, 96, 53-70.

Vespa, M., Lanson, M., and Manceau, A. (2010) Natural attenuation of zinc pollution in smelter-affected soil. Environmental Science & Technology, 44, 7814-7820.

Villalobos, M., Lanson, B., Manceau, A., Toner, B., and Sposito, G. (2006) Structural model for the biogenic Mn oxide produced by *Pseudomonas putida*. American Mineralogist, 91, 489-502.

Webb, S.M., Tebo, B.M., and Bargar, J.R. (2005) Structural characterization of biogenic Mn oxides produced in seawater by the marine *bacillus sp.* strain SG-1. American Mineralogist, 90, 1342-1357

Xu, H.F., Chen, T., and Konishi, H. (2010) HRTEM investigation of trilling todorokite and nano-phase Mn-oxides in manganese dendrites. American Mineralogist, 95, 556-562.

Yoshikawa, K. (1991) The relationship between manganese minerals and metallic elements in deep-sea manganese nodules. Marine Geology, 101, 267-286.

FIGURE CAPTIONS

Figure 1. Schematic representation of the topotactic transformation of 10Å-vernadite to todorokite. Tetravalent manganese cations likely occupy the central and edge sites of the triple chains from the todorokite framework, and the larger trivalent manganese and divalent nickel and copper cations the edge sites, exclusively (Post and Bish 1988; Post et al. 2003; Bodei et al. 2007).

Figure 2. Structural models for the two 10 Å-manganates, buserites-I and -II. Buserite-I is a two-water layer hydrate which transforms into the 7 Å-manganate birnessite after losing one water layer either in air, upon heating to 105-110 °C, or in vacuum. Buserite-II contains a high amount of interlayer cations above vacancy sites, which prevents it from collapsing to 7 Å. The structure models are adapted from Pal'chik et al. (2011). Note the unlikely absence of hydratation water bound to Na in Buserite-II.

Figure 3. Inner-sphere metal (Me) complexes at the δ-MnO_2 surface. E, DC, and TC refer to edge-, double-corner sharing, and triple-corner sharing complexes. The bidentate DC complex is located at the edge of the layer and the tridentate TC complex on the layer surface over a Mn vacancy. The E complex inside the Mn layer shares six edges with the surrounding MnO_6 octaheda.

Figure 4. EPMA analysis of trace metals and alkali and alkaline earth metal ions in the hydrogenetic-diagenetic nodule as a function of the Mn/Fe ratio. An Mn/Fe ratio of about 2.5 (vertical grey line) divides purely hydrogenetic regions from those that experienced the beginning of early diagenetic transformation (Halbach et al. 1981). Complete analyses are given in Supplementary Table1.

Figure 5. Synchrotron X-ray micro-fluorescence (SXRF) images of the distribution of trace metals and Fe and Mn in the hydrogenetic-diagenetic nodule (Map 1). The hydrogenetic region is to the left and the diagenetically transformed region to the right. Image size: 1484 (H) x 546 (V) μm^2, pixel size: 5 (H) x 5 (V) μm^2. In the Mn map (top left), the black areas correspond to ferruginous smectite.

Figure 6. Synchrotron X-ray micro-fluorescence (SXRF) images of the distribution of Cu, Fe, and Mn in a diagenetic vein and the surrounding hydrogenetic matrix (Map 2). Image size: 1350 (H) x 650 (V) μm^2, pixel size: 10 (H) x 10 (V) μm^2.

Figure 7. Scatter plots for MnKα and FeKβ fluorescence lines for the images shown in Figure 5 (Map 1) (**a**) and Supplementary Figure 2 (Map 3) (**b**). The pattern suggests that there are two chemically distinct populations of Fe. Complementary analysis by micro XRD and EXAFS indicate that Fe is associated with dioctahedral smectite in C (clay) areas and speciated as feroxyhite (δ-FeOOH) in H areas.

Figure 8. Representative micro XRD patterns (**a**) and point SXRF spectra (**b**) collected at 17 keV in the clay (C), hydrogenetic (H) and diagenetic (D) regions of the nodule. The C areas have major dioctahedral smectite, the H areas have major Fe-vernadite, and the diagenetic areas have variable

proportions of 10Å-vernadite (two-water layer phyllomanganate) and todorokite. The amount of todorokite increases as the hydrogenetic to diagenetic transformation increases (Supplementary Fig. 5). Peaks labeled V' correspond to the 001 and 002 reflection of pure vernadite crystallites with one-water layer (7 Å phyllomanganate). In vacuum or upon heating, the removal of one water layer from 10Å-vernadite causes the ~10 Å reflection to shift to ~ 7 Å (Supplementary Fig. 6) (Usui and Mita 1995; Manceau et al. 2007). Peaks labeled S, V, T, Fx, and F refer to smectite, vernadite, todorokite, feroxyhite, and feldspar, respectively.

Figure 9. (**a**) Mn K-edge XANES absorption spectra representative of the hydrogenetic and diagenetic regions. The spectra were normalized to unit step in the absorption coefficient from well below to well above the edge. (**b-f**) First derivatives compared to reference spectra (**b,e**), and Combo-fit to an extended database of reference spectra from Manceau et al. (2012) (**f**).

Figure 10. (**a,b**) Mn K-edge EXAFS spectra of the hydrogenetic nodule and triclinic (TcBi) hexagonal (HBi) birnessites and their Fourier transform magnitudes. The arrow at k = 8.1 $Å^{-1}$ denotes the double antinode pattern observed in some bioprecipitates (Webb et al. 2005), and resulting from the ordering of Mn^{3+} and Mn^{4+} in the phyllomanganate layer (Gaillot et al. 2003, 2007; Manceau et al. 2004). The arrow to the right denotes the shift to higher distances of the Mn-Mn peak in TcBi resulting from the presence of Mn^{3+} in the layer. The arrow at k = 6.5 $Å^{-1}$ points out the shoulder observed in HBi but absent in the sample because it lacks interlayer MnO_6 octahedra that share corners with the layer octahedra around vacancies (TC linkage). In real space, this is reflected by the absence of the Mn-Mn corner-sharing peak C. (**c,d**) Co K-edge EXAFS spectra and Fourier transform magnitudes of the hydrogenetic nodule (CoD465H) and two references, Co-sorbed birnessite (CoHBi74-4) and CoOOH. The sample has no corner-sharing Co-(Co,Mn) peak, meaning that all Co and Mn atoms are in the manganese layer. (**e,f**) Ni K-edge EXAFS spectra and Fourier transform magnitudes of the diagenetic nodule from the Central Pacific studied here (NiD465D), and from a hydrothermal metalliferous Fe-Mn deposit collected west of Nicoya Peninsula off Costa Rica (Ni50GCC) (Bodei et al. 2007, 2008; Steinmann et al. 2012). The crystal chemistry of Ni is nearly identical in the two deep-ocean Fe-Mn deposits. The Co- and Ni-EXAFS data are provided in the Supplementary material[1] as a useful resource for other studies.

Figure 11. Fourier transform magnitudes of Cu K-edge EXAFS data for crystalline birnessite and nanoparticulate δ-MnO_2 (synthetic vernadite, dBi) references. (**a**) Three birnessites with contrasted proportions of layer (E complex, peak B) and interlayer (TC complex, peak C) Cu^{2+}. (**b**) Two Cu-sorbed δ-MnO_2 samples showing the influence of sorption pH on the proportions of the layer and interlayer complexes. (**c**) Comparison of spectra for Cu-sorbed on birnessite and δ-MnO_2 showing that peak C is a doublet produced by Cu sorbed on layer vacancies (TC complex) and on layer edges (DC complex) (Fig. 3). This third complex is always present but only detected in δ-MnO_2 because Mn oxide nanosheets have a higher fraction of border sites. The Cu-EXAFS data are provided in the Supplementary material[1] as a useful resource for other studies.

Figure 12. Cu K-edge EXAFS spectra (**a**) and their Fourier transform magnitudes (**b**) representative of the structural forms of Cu in smectitic regions (CuD465H), in 10Å-vernadite from an early diagenetic region (diagenetic vein, CuD465D1), and in the diagenetic nodule with abundant todorokite (CuD465D2).

TABLE 1. Pearson *r* values for X-ray fluorescence intensities between elements, taken pixel-by-pixel. This correlation is a quantitative measure of the degree of association between two elements.

Map 1	Mn	Fe	Ce	Co	Ni	Cu	Pb
Mn	1						
Fe	-0.61	1					
Ce	-0.30	0.70	1				
Co	-0.16	0.77	0.59	1			
Ni	0.87	-0.74	-0.46	-0.37	1		
Cu	0.92	-0.75	-0.52	-0.38	0.92	1	
Pb	-0.03	0.59	0.69	0.70	-0.42	-0.25	1

Map 3	Mn	Fe	Ce	Co	Ni	Cu	Pb
Mn	1						
Fe	-0.51	1					
Ce	-0.23	0.62	1				
Co	-0.44	0.54	0.63	1			
Ni	0.78	-0.54	-0.27	-0.42	1		
Cu	0.89	-0.61	-0.39	-0.54	0.87	1	
Pb	-0.10	0.75	0.66	0.70	-0.36	-0.35	1

TABLE 2. List of Cu references

Mineral	Code name	pH	Cu/Mn*	Binding mechanism of Cu
Triclinic birnessite†	CuTcBi7-10	10	0.0074	Cu substituted for Mn in the octahedral layer (100 % E complex)
	CuTcBi7-6	6	0.0071	Cu in the layer (E complex) and interlayer (TC complex)
	CuTcBi7-4	4	0.0072	Cu in the layer (E complex) and interlayer (TC complex)
Hexagonal birnessite‡	CuHBi11-5	5	0.0112	Cu in the layer (E complex) and interlayer (TC complex)
	CuHBi5-5	5	0.0052	Cu in the layer (E complex) and interlayer (TC complex)
	CuHBi156-4	4	0.156	Cu predominantly in the interlayer (TC complex)
Vernadite§	CudBi12-7	7	0.0120	Cu in the layer, interlayer, and on layer edge (DC complex)
	CudBi3-5	5	0.0026	Cu in the layer, interlayer, and on layer edge (DC complex)

* Atomic ratio determined by wet chemical analysis following the procedure of Lanson et al. (2002b).

† TcBi was synthesized following the procedure of Giovanoli et al. (1970), as described by Drits et al. (1997) and Lanson et al. (2002a). TcBi was doped with Cu, then the pH 10 suspension (CuTcBi10-7) was equilibrated to pH 6 (CuTcBi7-6) and 4 (CuTcBi7-4). TcBi transforms to HBi at acidic pH (Silvester et al. 1997).

‡ The pH 5 samples were prepared by pre-equilibrating TcBi to the sorption pH to transform TcBi to HBi before the dropwise addition of $Cu(NO_3)_2$. The pH 4 sample was characterized previously by XRD (Lanson et al. 2002b) and EXAFS (Manceau et al. 2002a) (sample CuBi156). Cu sorption was achieved by adding $Cu(NO_3)_2$ while equilibrating the TcBi suspension to pH 4.

§ Synthesis (δ-MnO_2) and Cu sorption were performed following the procedure of Grangeon et al. (2012). δ-MnO_2 was pre-equilibrated at the sorption pH before the dropwise addition of $Cu(NO_3)_2$.

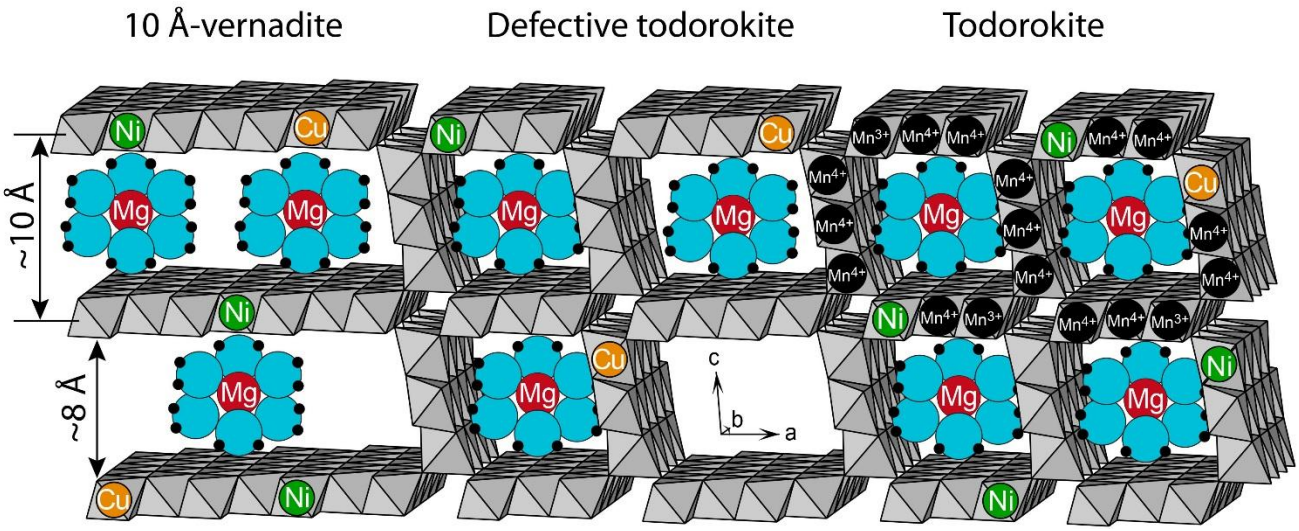
10 Å-vernadite
Defective todorokite
Todorokite
~10 Å
~8 Å
Ni
Cu
Mg
c
b
a
Mn3+
Mn4+

Figure 1

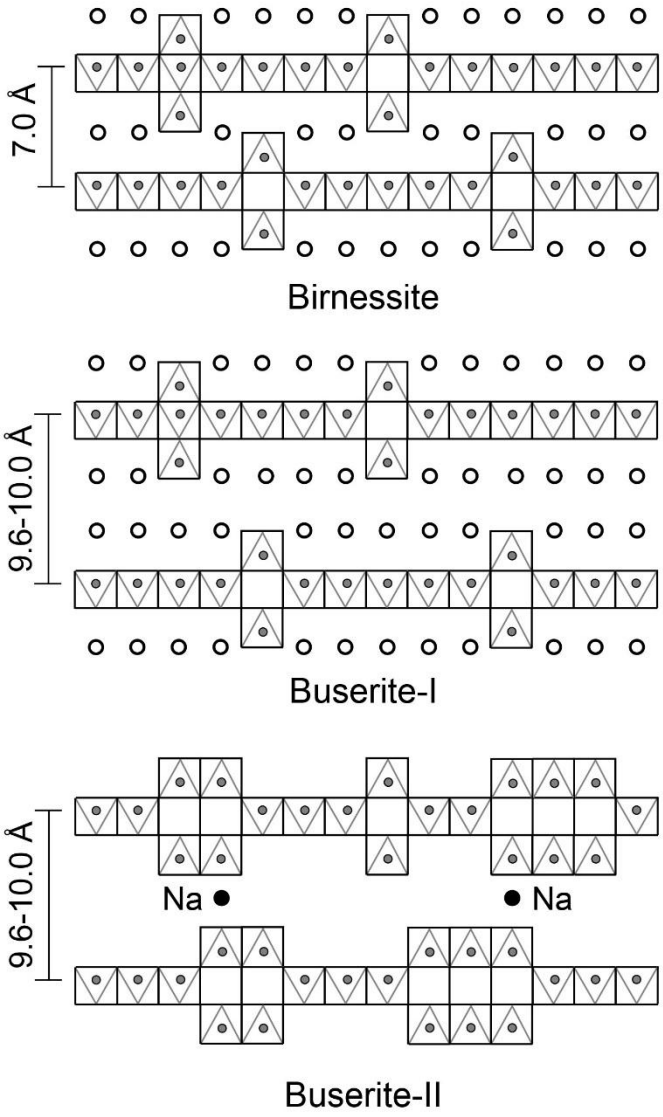

Figure 2

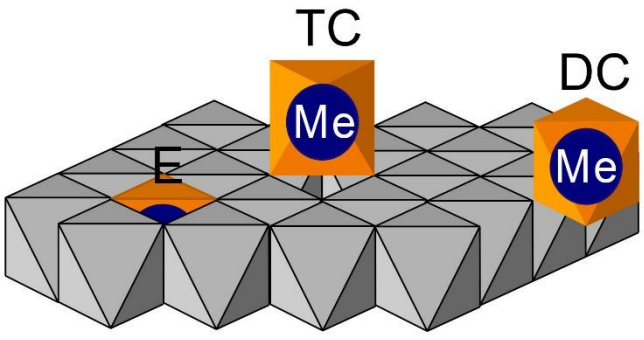

Figure 3

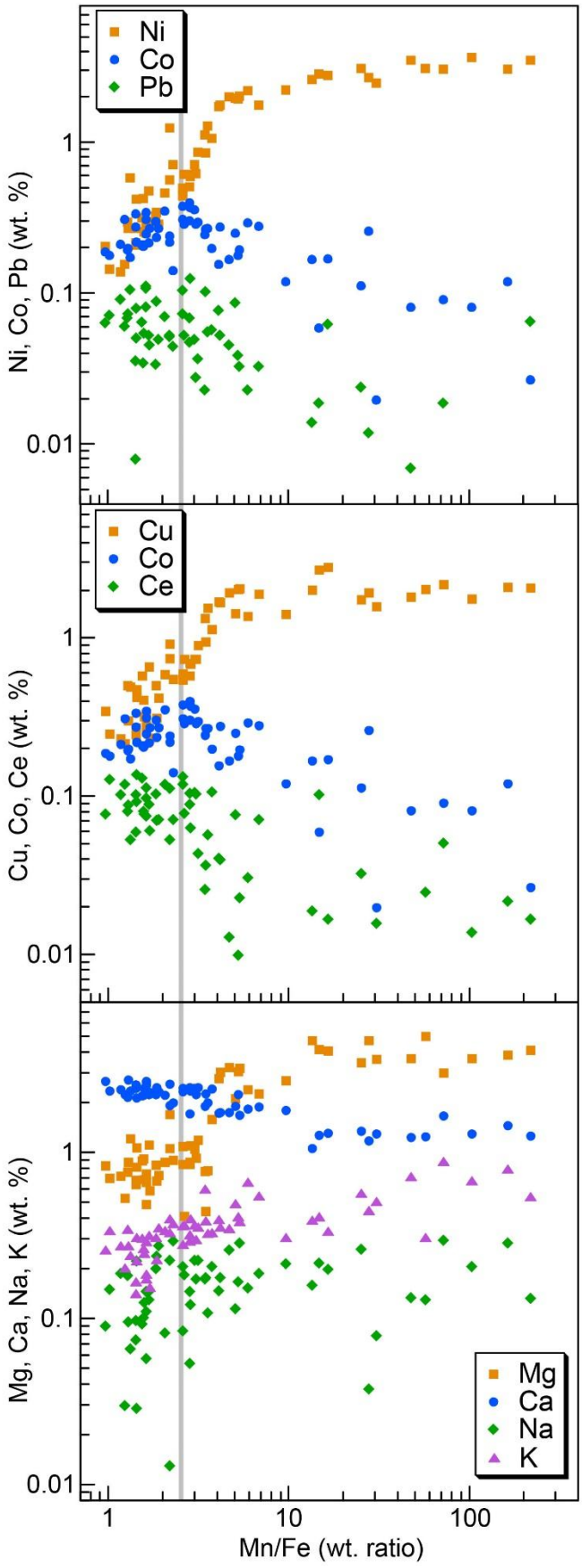
Ni
Co
Pb
Ni, Co, Pb (wt. %)
1
0.1
0.01
Cu
Co
Ce
Cu, Co, Ce (wt. %)
1
0.1
0.01
Mg
Ca
Na
K
Mg, Ca, Na, K (wt. %)
1
0.1
0.01
1
10
100
Mn/Fe (wt. ratio)

Figure 4

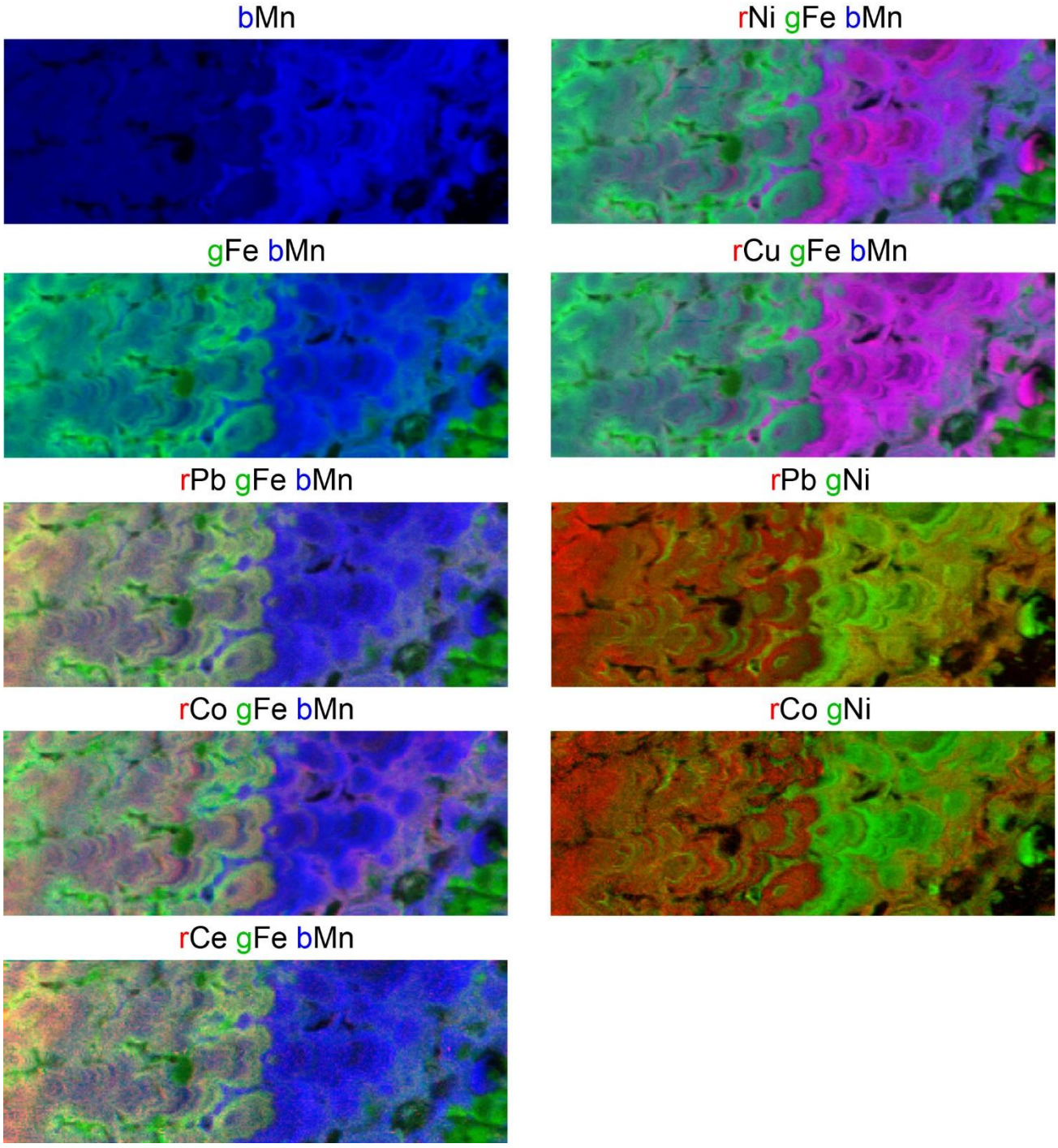
bMn
rNi gFe bMn
gFe bMn
rCu gFe bMn
rPb gFe bMn
rPb gNi
rCo gFe bMn
rCo gNi
rCe gFe bMn

Figure 5

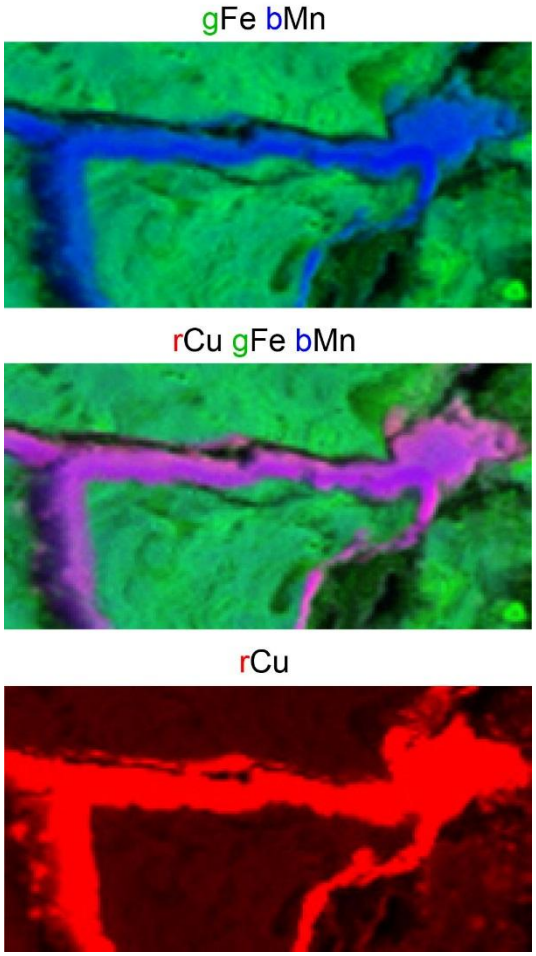

Figure 6

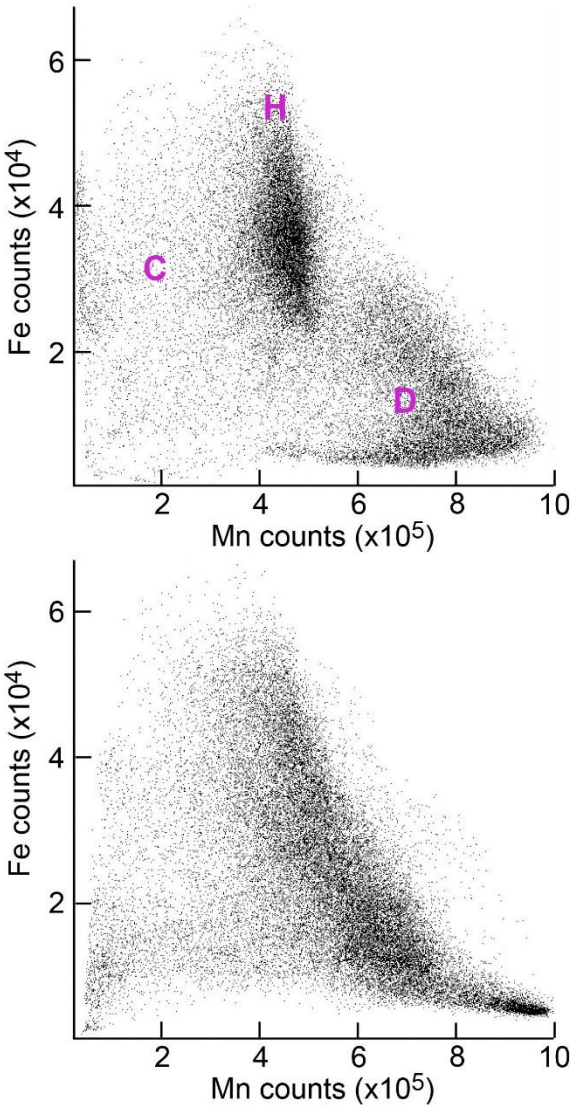

Figure 7

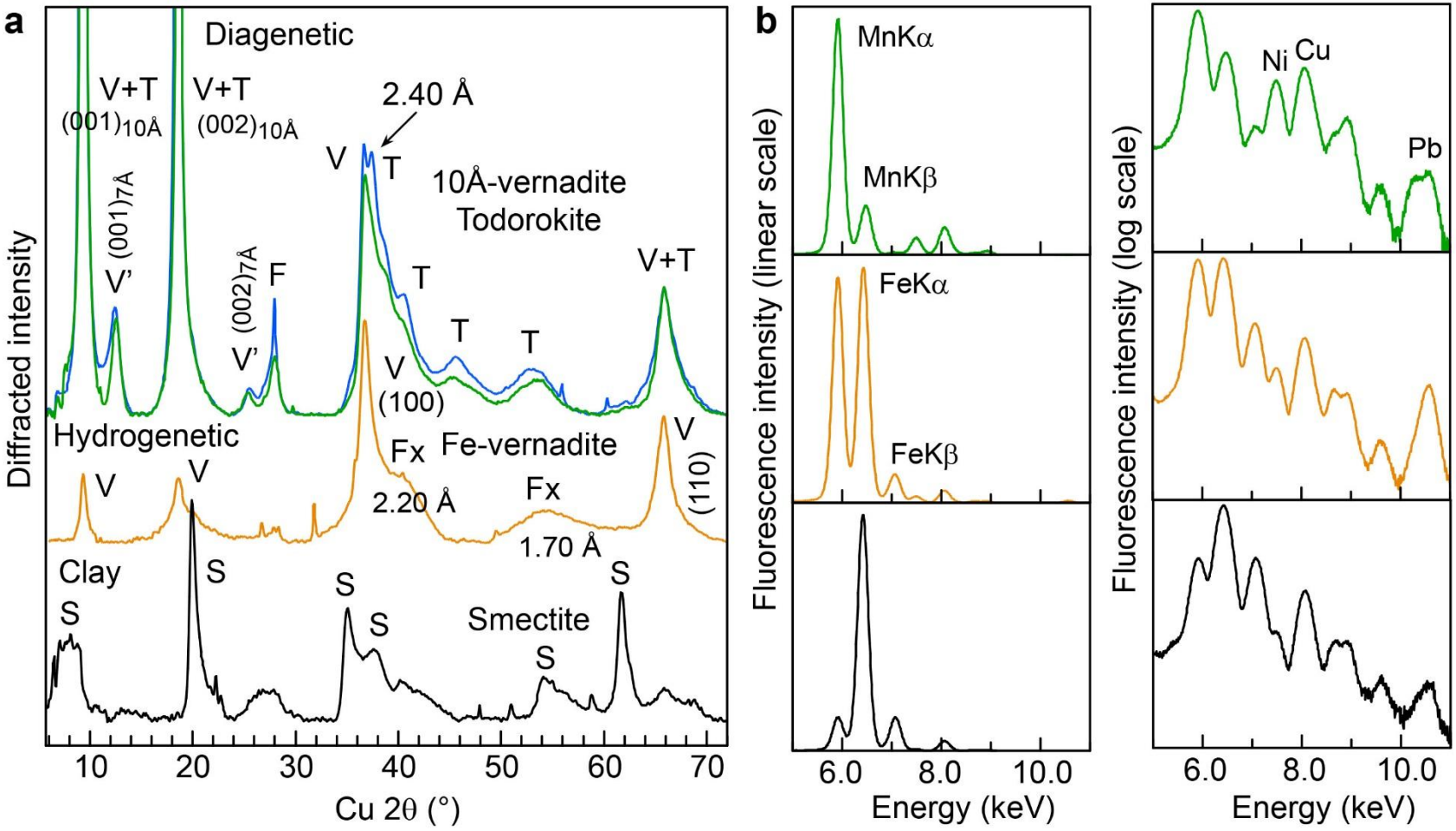
a
Diagenetic
V+T
(001)10Å
V+T
(002)10Å
2.40 Å
V
T
10Å-vernadite
Todorokite
V'
(001)7Å
V'
(002)7Å
F
T
T
T
V+T
V
(100)
Hydrogenetic
Fx
Fe-vernadite
V
V
2.20 Å
Fx
V
(110)
1.70 Å
Clay
S
S
S
S
Smectite
S
S
Diffracted intensity
10
20
30
40
50
60
70
Cu 2θ (°)
b
MnKα
MnKβ
FeKα
FeKβ
Fluorescence intensity (linear scale)
Ni
Cu
Pb
Fluorescence intensity (log scale)
6.0
8.0
10.0
Energy (keV)
6.0
8.0
10.0
Energy (keV)

Figure 8

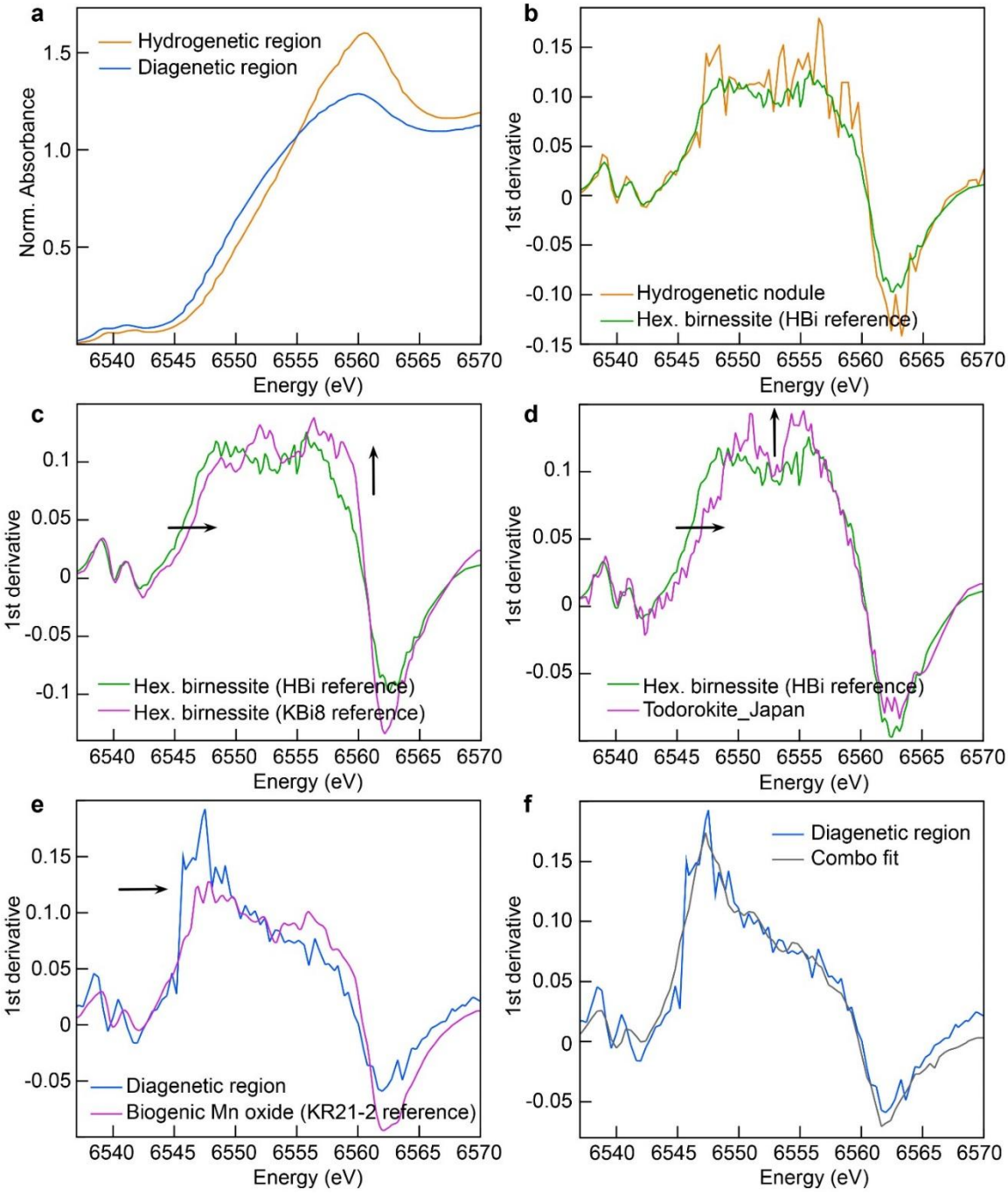
a
Hydrogenetic region
Diagenetic region
Norm. Absorbance
Energy (eV)
b
1st derivative
Hydrogenetic nodule
Hex. birnessite (HBi reference)
Energy (eV)
c
1st derivative
Hex. birnessite (HBi reference)
Hex. birnessite (KBi8 reference)
Energy (eV)
d
1st derivative
Hex. birnessite (HBi reference)
Todorokite_Japan
Energy (eV)
e
1st derivative
Diagenetic region
Biogenic Mn oxide (KR21-2 reference)
Energy (eV)
f
1st derivative
Diagenetic region
Combo fit
Energy (eV)

Figure 9

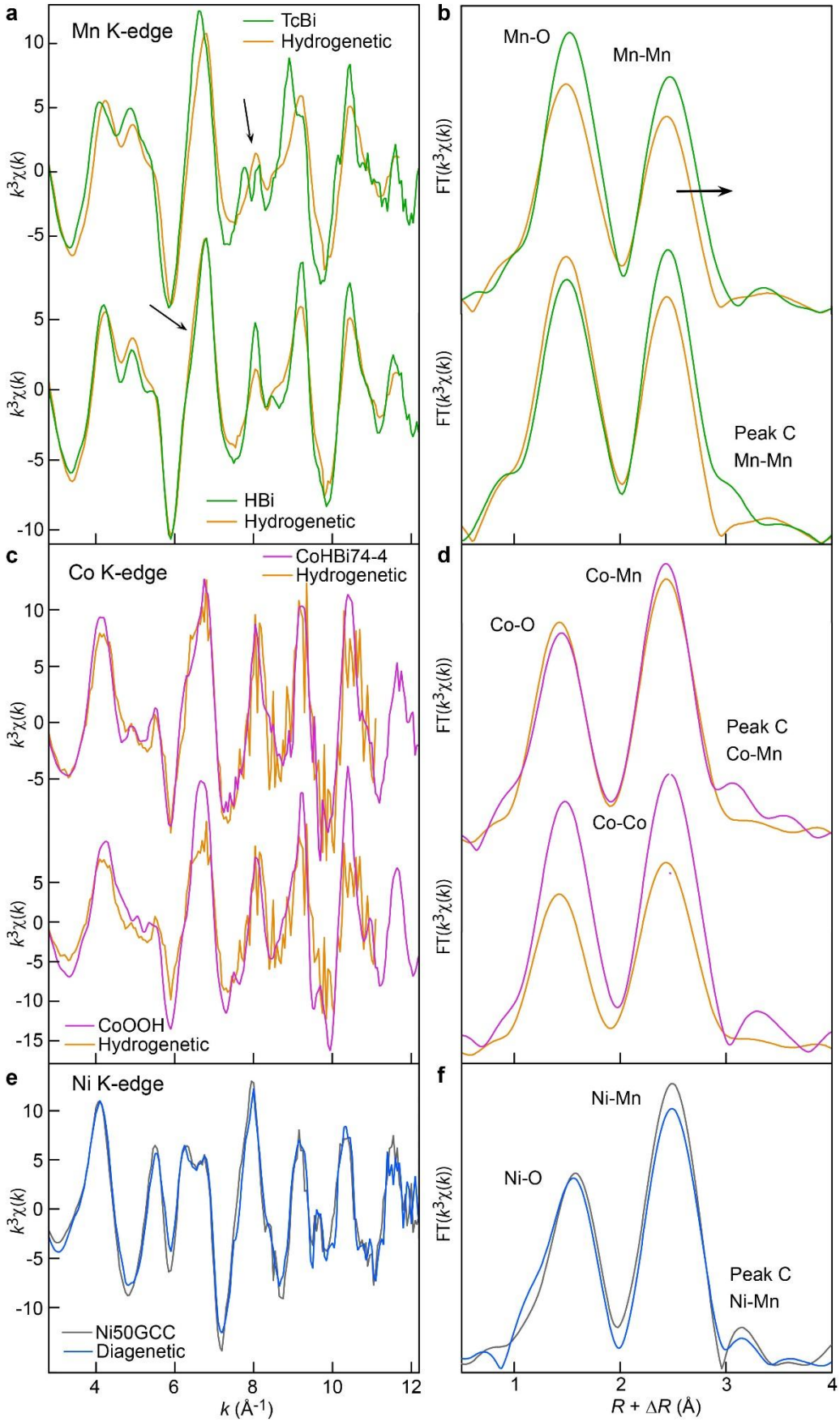
a
Mn K-edge
TcBi
Hydrogenetic
HBi
Hydrogenetic
b
Mn-O
Mn-Mn
Peak C
Mn-Mn
c
Co K-edge
CoHBi74-4
Hydrogenetic
CoOOH
Hydrogenetic
d
Co-Mn
Co-O
Peak C
Co-Mn
Co-Co
e
Ni K-edge
Ni50GCC
Diagenetic
f
Ni-Mn
Ni-O
Peak C
Ni-Mn
k (Å-1)
R + ΔR (Å)

Figure 10

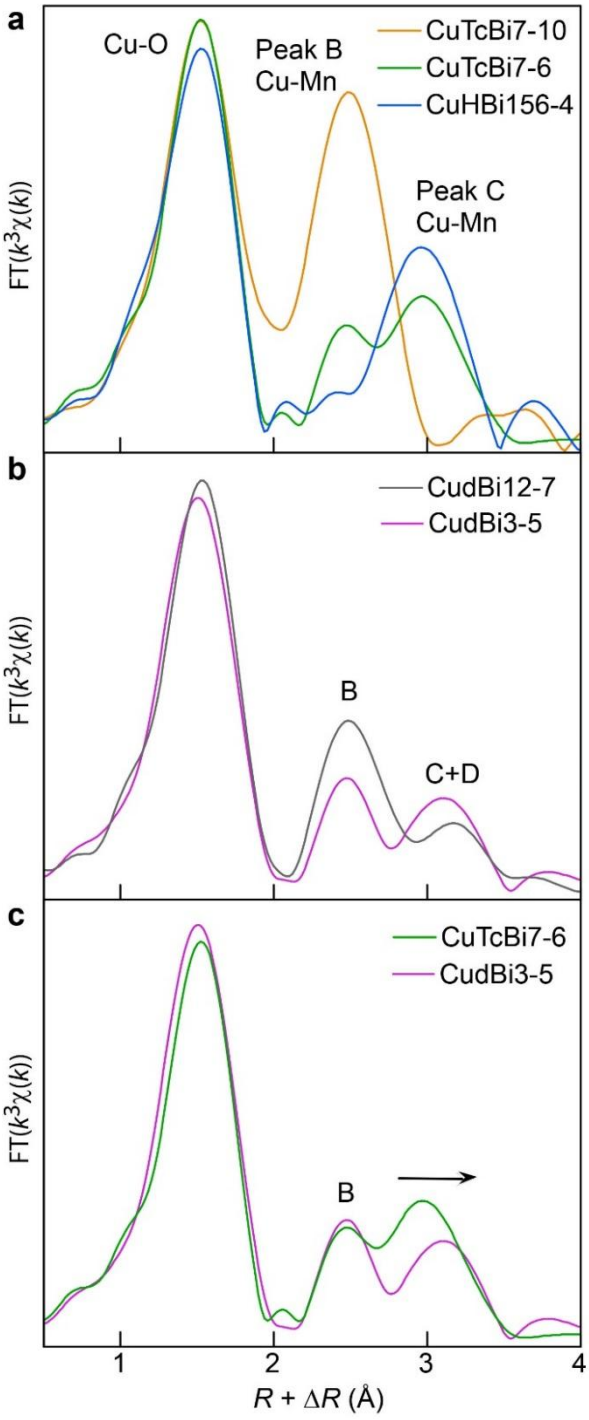
a
Cu-O
Peak B
Cu-Mn
CuTcBi7-10
CuTcBi7-6
CuHBi156-4
Peak C
Cu-Mn
FT(k3χ(k))
b
CudBi12-7
CudBi3-5
B
C+D
FT(k3χ(k))
c
CuTcBi7-6
CudBi3-5
B
FT(k3χ(k))
1
2
3
4
R + ΔR (Å)

Figure 11

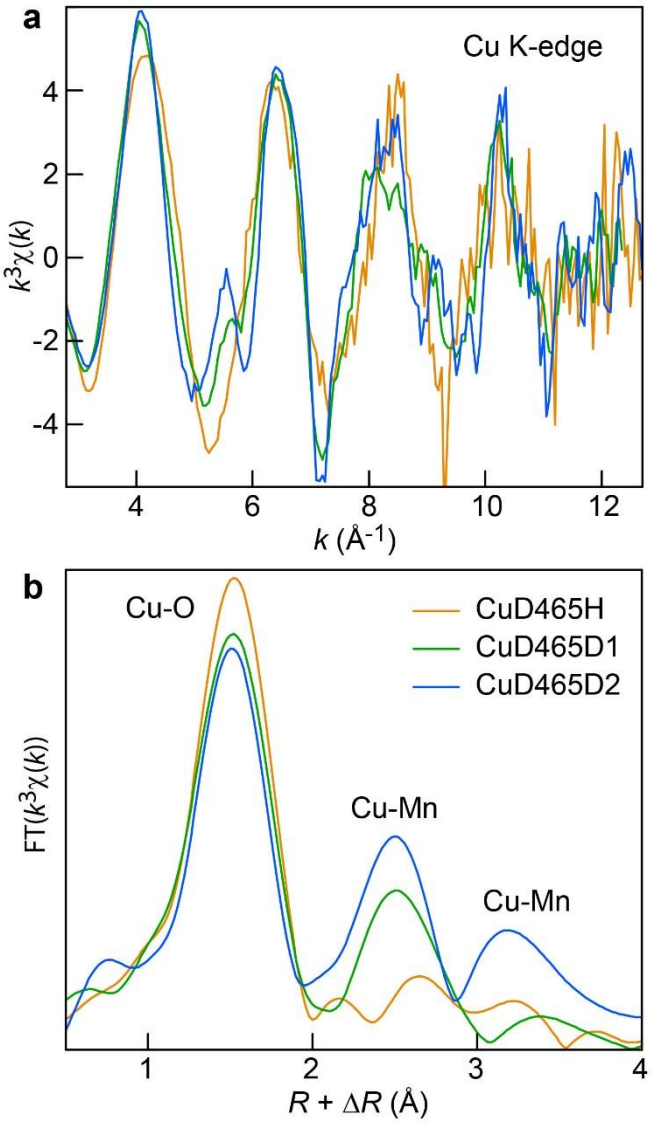
a
Cu K-edge
4
2
0
-2
-4
$k^3\chi(k)$
4
6
8
10
12
k (Å^{-1})
b
Cu-O
CuD465H
CuD465D1
CuD465D2
Cu-Mn
Cu-Mn
FT($k^3\chi(k)$)
1
2
3
4
$R + \Delta R$ (Å)

Figure 12

Supplementary materials for the article

Mineralogy and crystal chemistry of Mn, Fe, Co, Ni, and Cu in a deep-sea Pacific polymetallic nodule

ALAIN MANCEAU[1,*] MARTINE LANSON[1] AND YOSHIO TAKAHASHI[2]

[1]ISTerre, Univ. Grenoble Alpes and CNRS, F-38041 Grenoble, France.

[2]Institute for Sustainable Sciences and Development, Hiroshima University, 1-3-1 Kagamiyama, Higashi-Hiroshima 739-8526, Japan

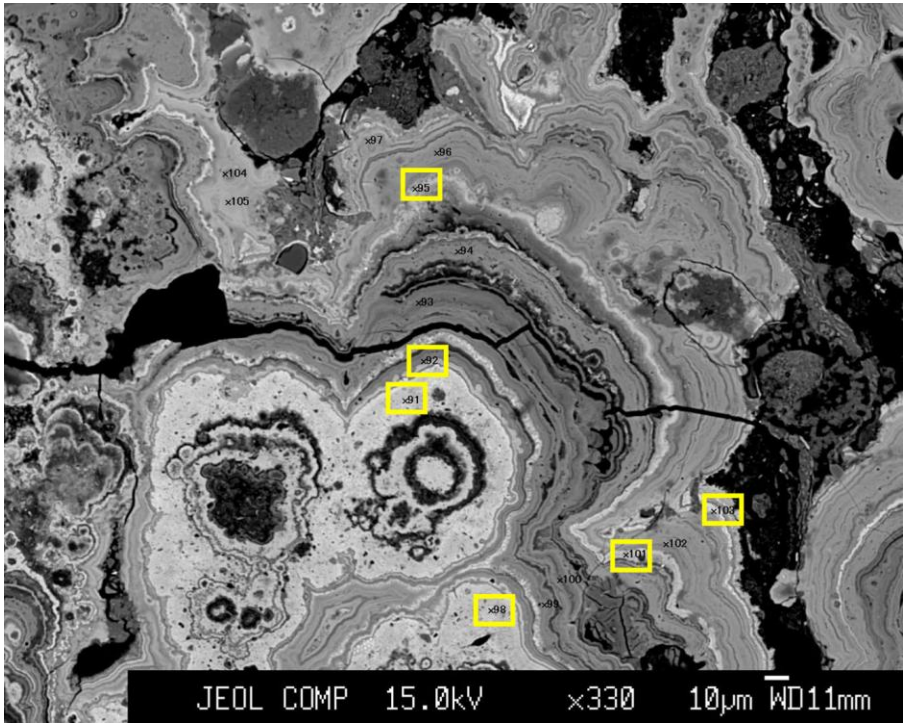

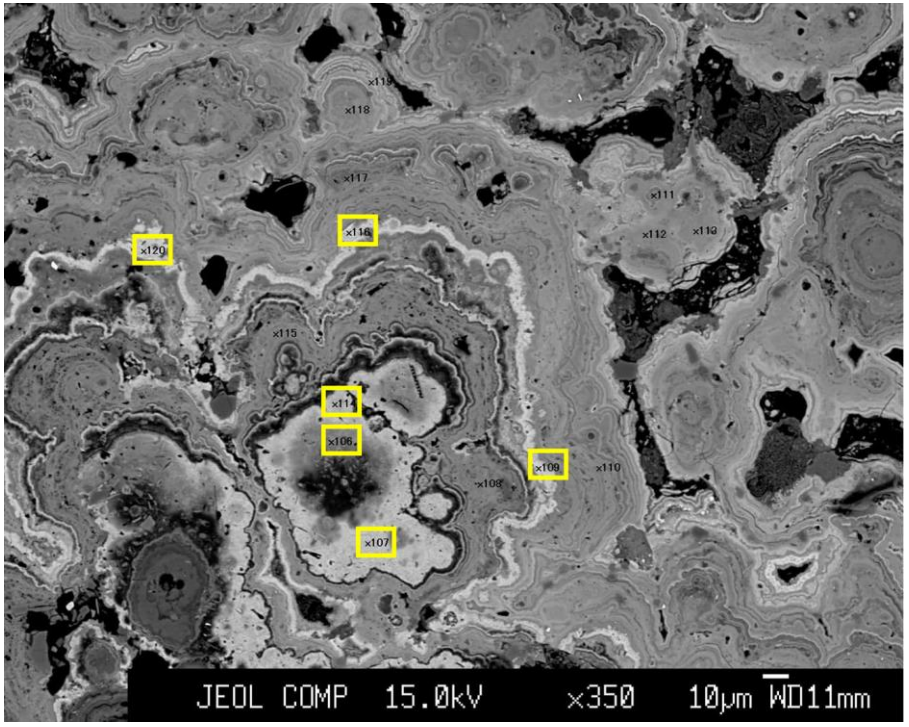

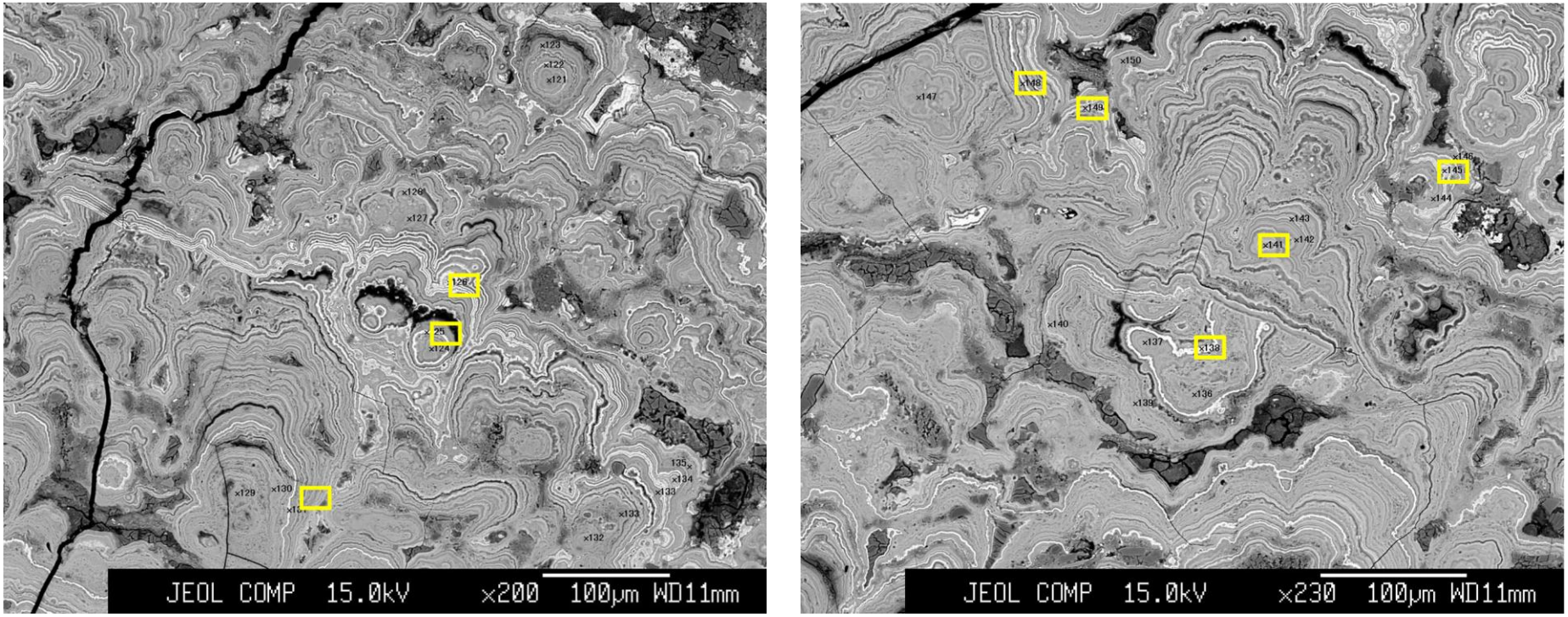

Figure S1. Surveys of the hydrogenetic-diagenetic growth discontinuity of the Fe-Mn nodule using backscattered electron images. This allows identification of Fe- and Mn-oxide phases that differ in brightness in the backscattered electron images. Black areas are voids, dark gray areas are clay phases, opaque gray areas are hydrogenetic regions, and bright gray areas are diagenetic regions. The analyzed spots are indicated with numbers and results are reported in Table S1 and the Supplementary material. The diagenetic spots are surrounded with yellow boxes. Image sizes are 360 (H) x 260 (V) μm^2 for the top two, and 530 (H) x 420 (V) μm^2 for the two below. Electron beam size is about 0.5-1.0 µm.

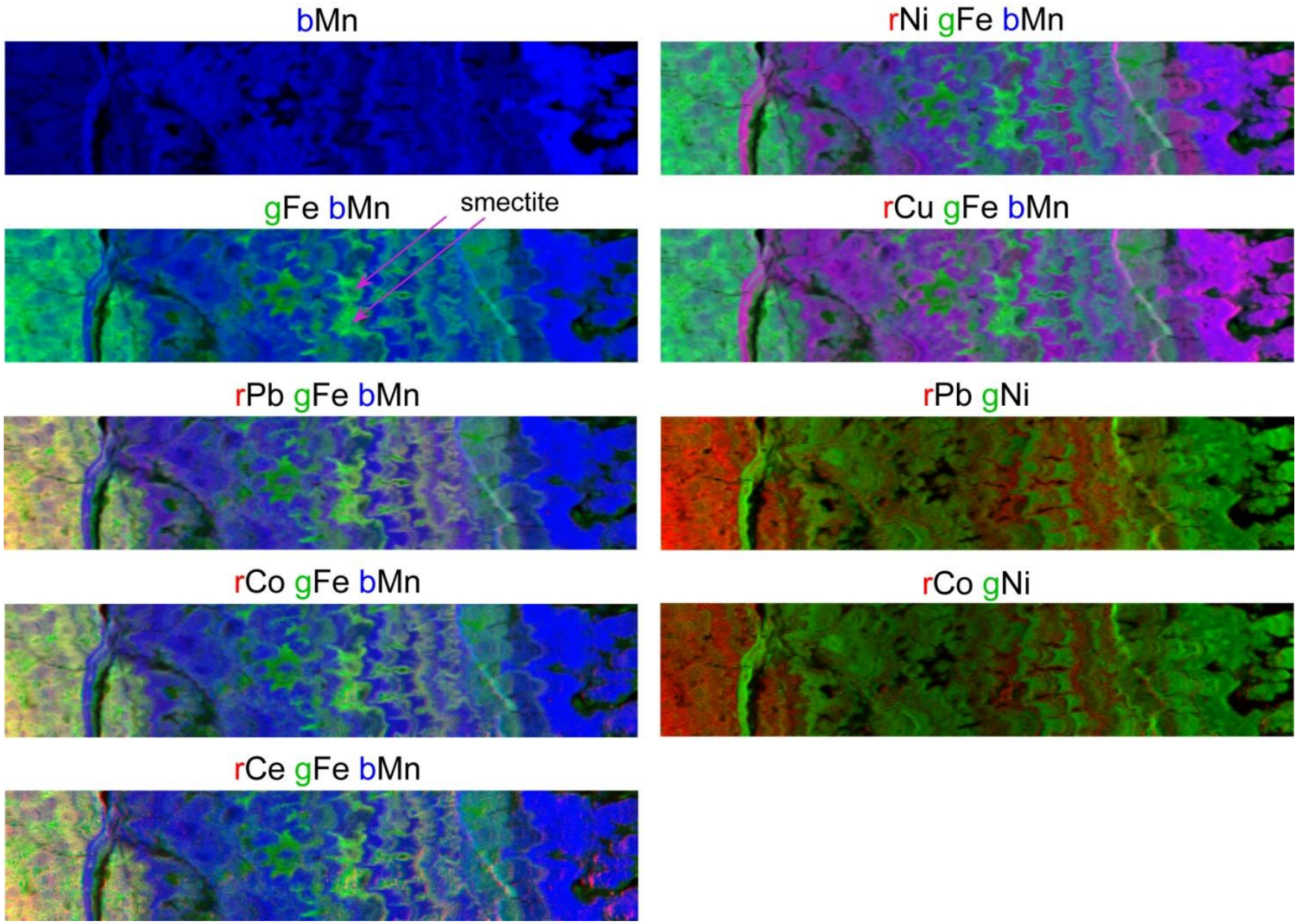

Figure S2. Synchrotron X-ray micro-fluorescence (SXRF) images of the distribution of trace metals and Fe and Mn in the hydrogenetic-diagenetic nodule (Map 3). The hydrogenetic region is to the left and the diagenetic region to the right. Two large smectite areas are indicated with arrows. Image size: 5910 (H) x 1250 (V) μm^2, pixel size: 15 (H) x 15 (V) μm^2.

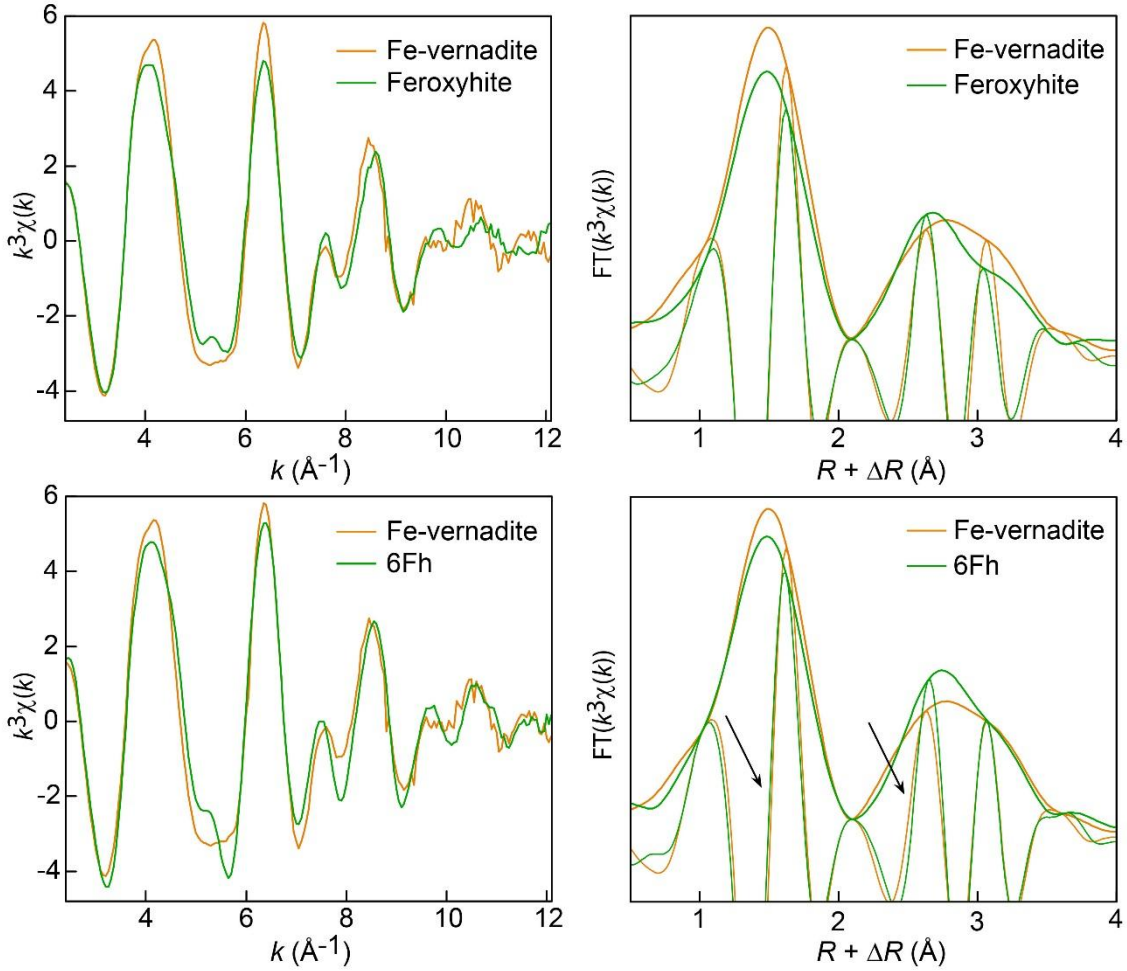

Figure S3. Fe K-edge EXAFS spectra and their Fourier transforms for Fe-vernadite and two models, feroxyhite (δ-FeOOH) and six-line ferrihydrite (6Fh). The magnitudes and imaginary parts of the Fourier transforms are shown. The small shifts in distance are more reliably detected by looking at the imaginary part than the magnitude. Arrows point out the phase difference in the Fourier transforms between the sample and 6Fh. The spectrum of Fe-vernadite is distinct from those of well-crystallized Fe oxyhydroxides (e.g., α- and β-FeOOH).

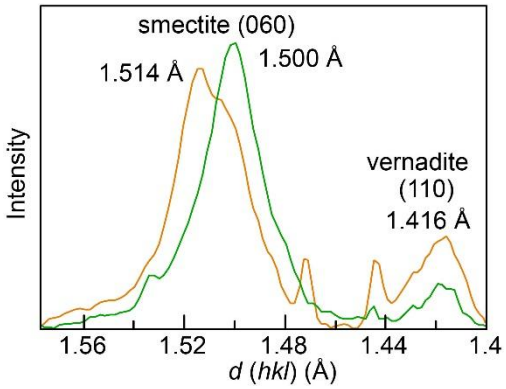

Figure S4. Two high-angle micro XRD patterns taken in clay-rich regions of the nodule showing the (060) reflection of the clay and the (110) reflection of vernadite. The 1.500 Å reflection identifies an aluminous smectite, and the 1.514 Å reflection an Fe-Al dioctahedral smectite.

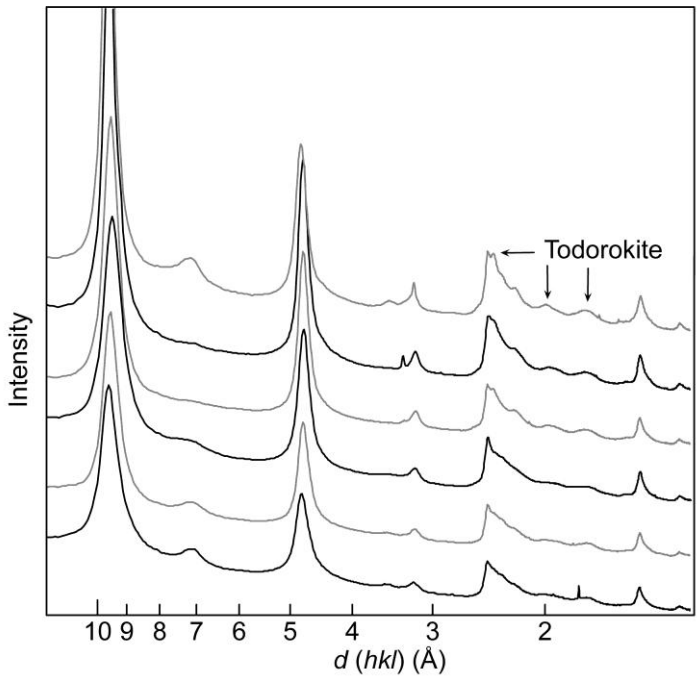

Figure S5. Micro-XRD patterns taken in the diagenetic nodule at different stages of the hydrogenetic to diagenetic transformation, as indicated by the increasing amount and crystallinity of todorokite. The simultaneous reinforcement of the basal reflection comes from the topotactic transition of 10Å-vernadite to todorokite (Bodei et al. 2007).

Figure S6 below is a compilation of XRD patterns from marine manganese oxides recorded at room condition and after in-situ vacuum dehydration. Some dehydrated samples were rehydrated in-situ in air at room temperature for several hours and a new pattern recorded.

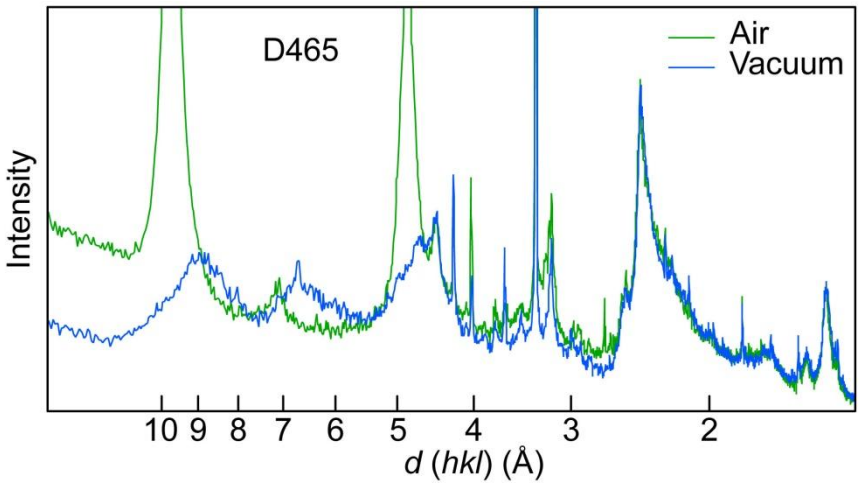

Figure S6a. XRD pattern of the D465 nodule in the hydrated and dehydrated state. Under vacuum, the composite (001) reflection from 10Å-vernadite splits into one reflection at ~8.9 Å from todorokite, and another at 6.5-7.0 Å from 7Å-vernadite (turbostratic birnessite). HRTEM imaging shows that 10Å-vernadite is a complex intergrowth of nano-sized domains of todorokite and vernadite (Bodei et al. 2007). The two types of crystallites are revealed upon dehydration.

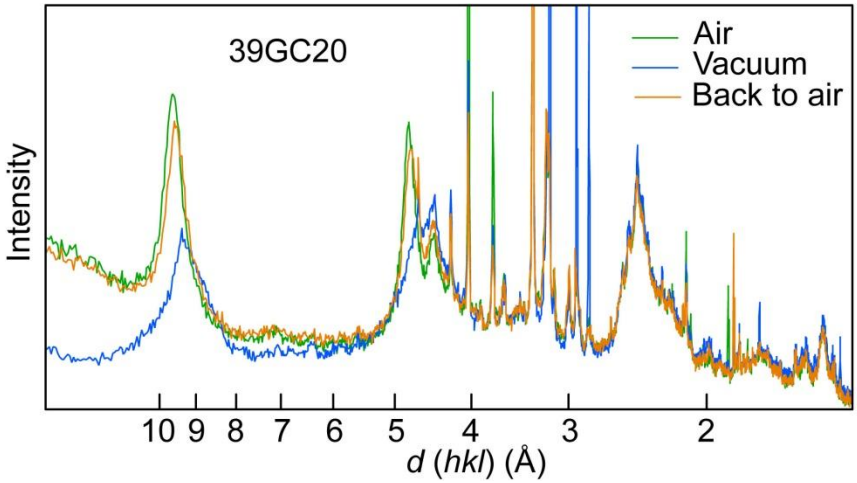

Figure 6b. XRD pattern of a manganese oxide (39GC20) collected near the 50GCC sample during the Ticoflux II cruise (2001) on the eastern flank of the East Pacific Rise (EPR) offshore Costa Rica (Courtesy of Dr. M. Buatier). The Mn oxide is almost pure todorokite. The narrow reflections are from quartz, anorthite and calcite.

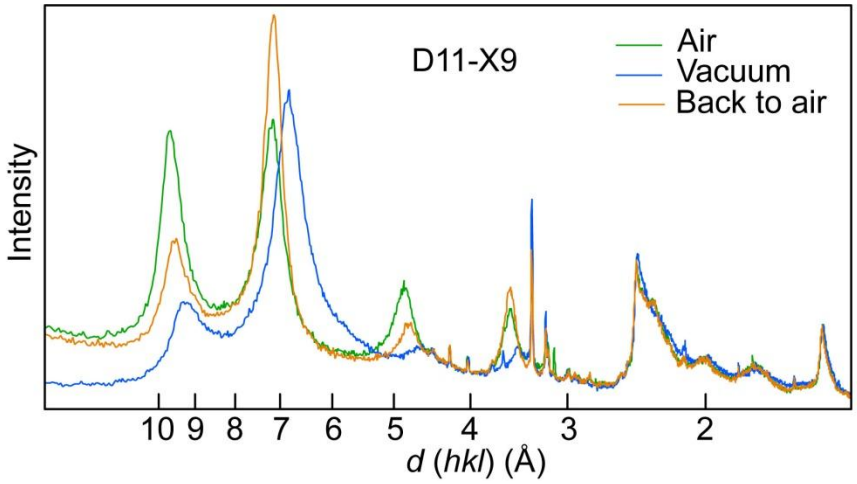

Figure S6c. XRD pattern of a manganese oxide (D11-X9) collected in an hydrothermal field in NW Pacific Ocean at 1575 m depth (Takahashi et al. 2007). Todorokite, 10Å-vernadite, and 7Å-vernadite comprise the majority of the sample. The weak reflection at 2.33 Å is from hexagonal birnessite, as shown below for sample D12-X2 collected in close proximity to D11-X9.

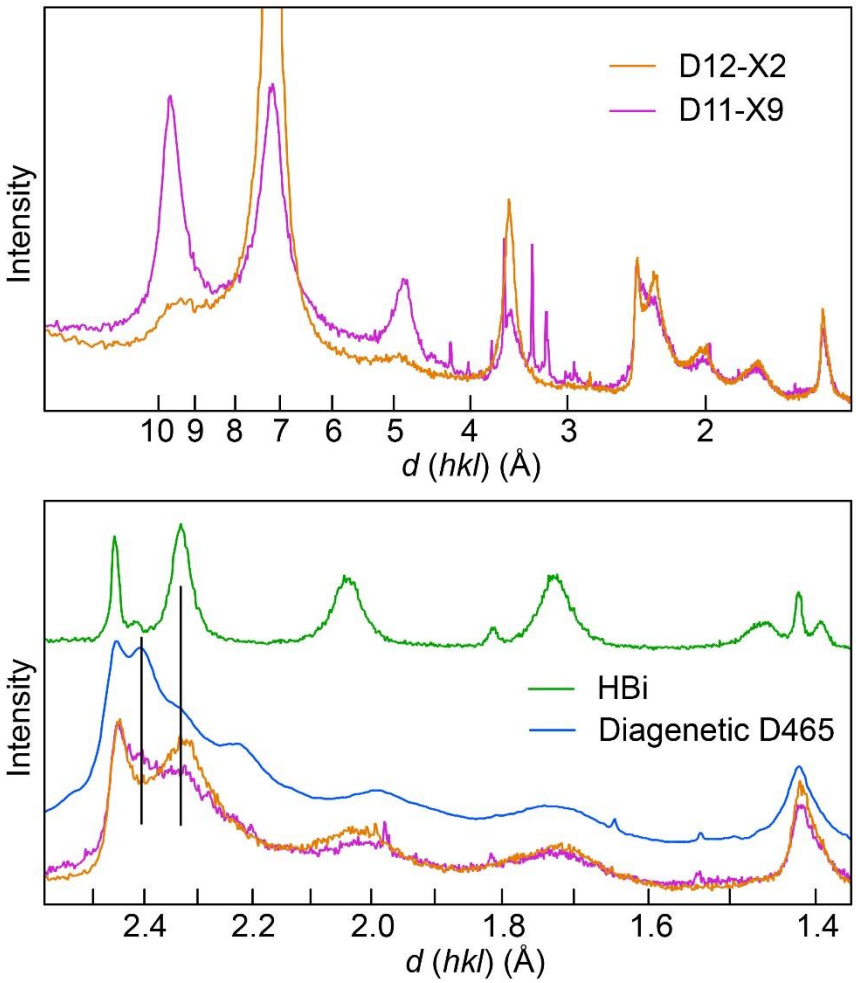

Figure S6d. XRD pattern of a manganese oxide (D12-X2), collected in the same hydrothermal field as D11-X9, compared to the patterns of D11-X9, synthetic hexagonal birnessite (Drits et al. 1997), and the micro-XRD pattern of 10Å-vernadite + todorokite shown in Figure 8a (diagenetic D465). The mineral composition of D12-X2 comprises todorokite, 10Å-vernadite, 7Å-vernadite, and hexagonal birnessite. The disordered 7Å-vernadite and ordered birnessite crystallites are probably interlayered (Lanson et al. 2000). All patterns were recorded in air.

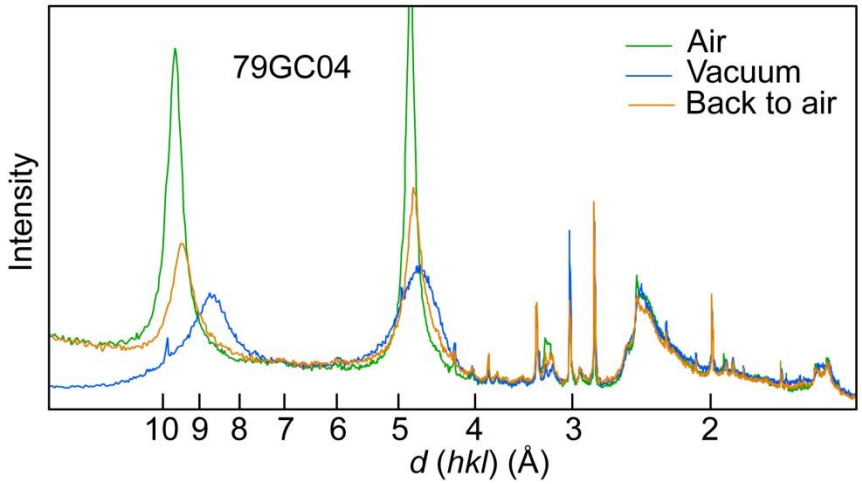

Figure S6e. XRD pattern of a manganese oxide **(**79GC04) collected in an hydrothermal field from the flank of the Juan de Fuca Ridge (Buatier et al. 2004). The Mn oxide is a turbostratic asbolane. This mixed-layer mineral is identified by the strong (002) reflection, which has a higher intensity than the (001) reflection, and a split of the two *hk*0 reflections. The intense (002) reflection indicates that the phyllomanganate interlayer contains an ordered layer from a metal (oxy)hydroxide, such as $Ni(OH)_2$, $Co(OH)_2$, $Cu(OH)_2$, or $Mn(OH)_2$ in the case of asbolane, or Al(OOH in the case of lithiophorite. The sub-lattices of the two interstratified layers are incommensurate in both the *a* and *b* directions, as indicated by the split of the (100) and (110) reflections (Chukhrov et al. 1980; Manceau et al. 1992).

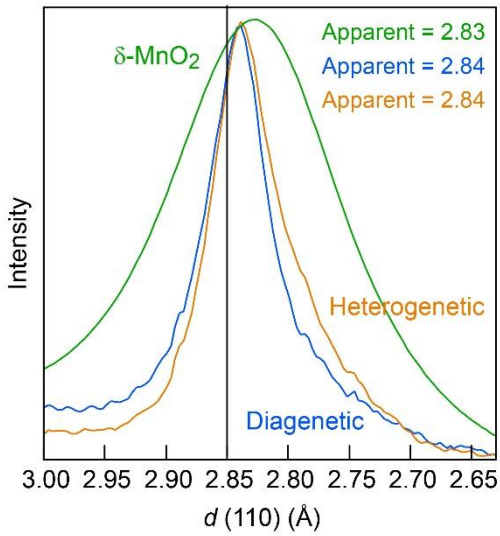

Figure S7. Profile of the (110) reflection of the nodule vernadite measured in the hydrogenetic and diagenetic regions (enlarged patterns from Fig. 8) compared to δ-MnO_2 equilibrated at pH 10 (Manceau et al. 2013). The three materials have a *b* value of 2.85 Å, but their peak maximum is shifted to lower 2x*d*(*hkl*) values in small particles to a greater extent the smaller the layer size.

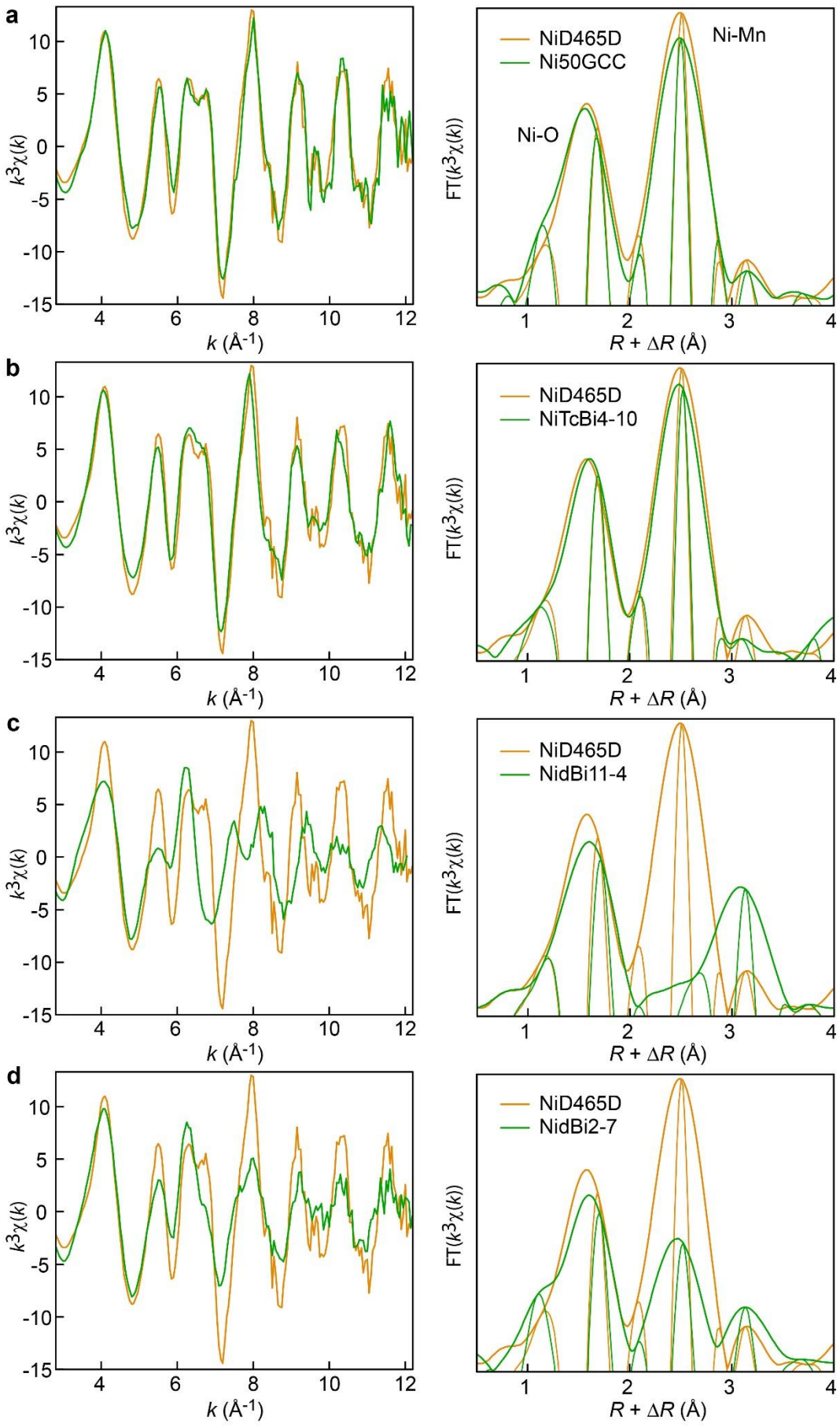
a
b
c
d
$k^3\chi(k)$
k (Å^{-1})
FT($k^3\chi(k)$)
$R + \Delta R$ (Å)
NiD465D
Ni50GCC
Ni-O
Ni-Mn
NiTcBi4-10
NidBi11-4
NidBi2-7

Figure S8. Ni K-edge EXAFS spectra and the magnitude and imaginary part of their Fourier transforms for the diagenetic nodule (NiD465D) and different models. (**a**) Mn deposit in hemipelagic sediments off Costa Rica from Bodei *et al.* (2007), in which Ni is partitioned among 10Å-vernadite and todorokite (Ni50GCC). (**b**) Ni incorporated in the MnO_2 layer of triclinic birnessite, similarly to Cu in CuTcBi7-10 (NiTcBi4-10). The Ni-O and Ni-Mn distances are a little longer in TcBi than in vernadite because TcBi has more Mn^{3+} (Manceau et al. 2005). (**c**,d) Ni-sorbed on δ-MnO_2 at pH 4 (Ni/Mn = 0.011; NidBi11-4) and pH 7 (Ni/Mn = 0.002 ; NidBi2-7) (Manceau et al. 2007). Ni is predominantly above vacancies in NidBi11-4 (TC complex, peak C), and occupies also layer vacancy sites in NidBi2-7 (peak B).

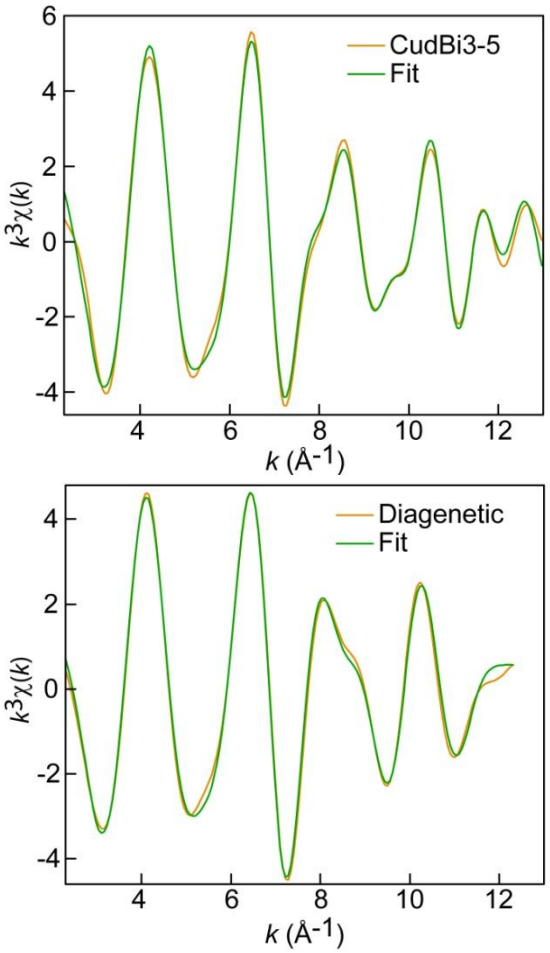

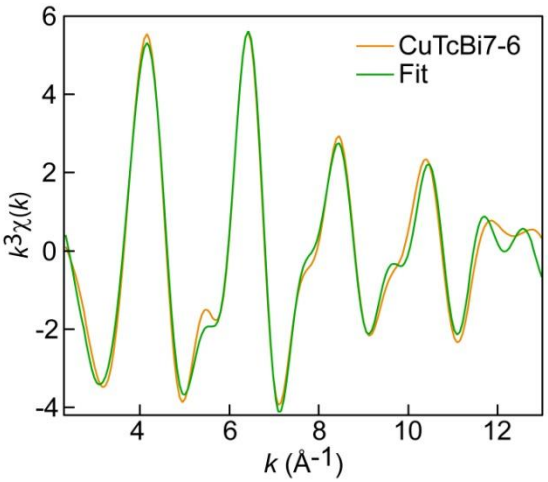

Figure S9. Multi-shell fit to Fourier-filtered Cu-O and Cu-Mn EXAFS data for CudBi3-5, CuTcBi7-6, and Cu in the diagenetic nodule D465. The fit parameters are listed in Table S2. The poorer simulation of CuTcBi7-6 comes from the omission in the fit of edge sites (DC complex) at about 3.68 Å. Although detected, their contribution is too weak to achieve stable solutions.

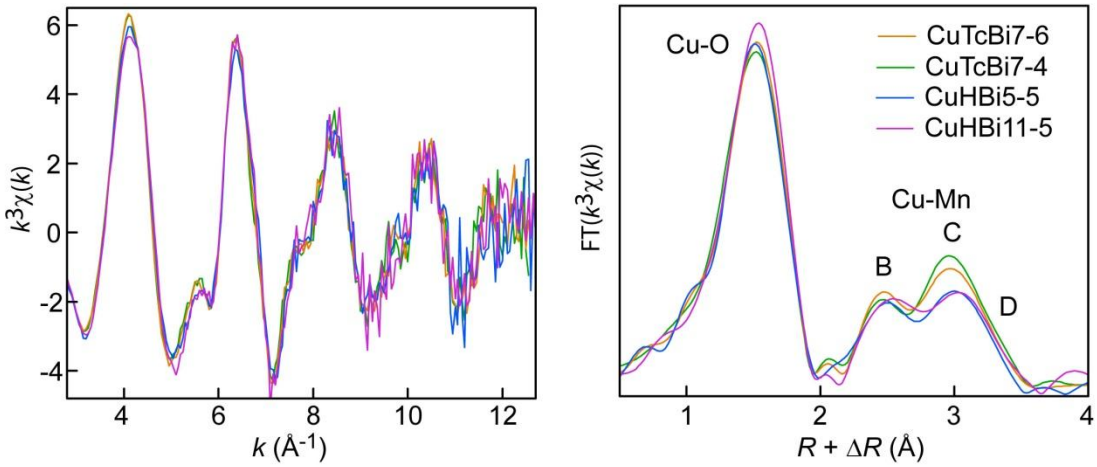

Figure S10. Cu K-edge EXAFS spectra and their Fourier transforms for Cu sorbed and incorporated in birnessite as a function of the equilibrium pH and sample preparation. Cu was coprecipitated with Mn in triclinic birnessite (TcBi) at pH 10 and the TcBi suspension subsequently equilibrated at pH 6 (CuTcBi7-6) or 4 (CuTcBi7-4). At acidic pH, TcBi is transformed to hexagonal birnessite (HBi). The two HBi samples were prepared by pre-equilibrating a TcBi suspension to pH 5 and the Cu sorbed at this pH directly on HBi. The synthesis route has little effect on the Cu partitioning among the layer site (E complex, peak B), interlayer site (TC complex, peak C), and edge site (DC complex, peak D). TcBi has a higher proportion of TC complex because its layers have a larger dimension.

Table S1. Mn/Fe ratios and trace metal concentrations (wt. %) shown in Figure 4 as measured by EPMA. The complete chemical analyses are given in the Supplementary material. The exact location of each analyzed spot is indicated on the backscattered electron images. The counting time was 40 s for the Ce and Pb fluorescence peaks and 2 x 20 s for the background counts measured on each side of the fluorescence peaks. These numbers are 20 s and 2 x 10 s for the other elements. The relative standard deviation (RSD) calculated from the total counts are 2% for Mg, Ca, Mn, and Fe, 6% for Ni and Cu, 20% for Na and Co, and 60% for Ce and Pb.

Spot #	Mn/Fe	Co	Ni	Cu	Ce	Pb	Mg	Ca	Na
91	160.87	0.121	3.096	2.127	0.022	-	3.912	1.466	0.286
92	9.51	0.121	2.262	1.428	0.000	-	2.729	1.815	0.214
93	1.60	0.350	0.255	0.259	0.098	0.109	0.491	2.651	0.111
94	1.23	0.313	0.157	0.217	0.120	0.061	0.534	2.266	0.030
95	27.51	0.263	2.728	1.946	0.000	0.012	4.780	1.181	0.038
96	1.41	0.278	0.218	0.248	0.060	0.008	0.685	2.457	0.075
97	1.31	0.175	0.587	0.495	0.054	0.107	1.222	2.374	0.066
98	71.33	0.092	3.084	2.211	0.051	0.019	3.023	1.681	0.297
99	2.26	0.143	0.721	0.555	0.072	0.045	0.906	2.003	0.294
100	1.84	0.238	0.348	0.316	0.071	0.089	0.677	2.492	0.238
101	13.36	0.170	2.629	2.040	0.019	0.014	4.779	1.067	0.160
102	1.60	0.252	0.280	0.336	0.076	0.082	0.752	2.562	0.146
103	5.86	0.296	2.221	1.380	0.031	0.023	2.415	1.842	0.154
104	1.27	0.200	0.273	0.304	0.089	0.074	0.885	2.749	0.096
105	0.95	0.190	0.207	0.348	0.078	0.064	0.841	2.699	0.091
106	30.16	0.020	2.508	1.596	0.016	0.001	3.691	1.303	0.079
107	216.50	0.027	3.550	2.104	0.017	0.066	4.186	1.274	0.133
108	1.41	0.339	0.274	0.275	0.103	0.036	0.650	2.570	0.098
109	47.15	0.082	3.535	1.828	0.000	0.007	3.726	1.241	0.135
110	1.57	0.212	0.259	0.323	0.078	0.055	0.695	2.464	0.126

111	1.55	0.207	0.430	0.409	0.081	0.035	0.921	2.243	0.102
112	1.00	0.182	0.146	0.252	0.129	0.072	0.706	2.379	0.151
113	1.16	0.215	0.141	0.233	0.103	0.092	0.725	2.401	0.189
114	56.68	0.001	3.116	2.061	0.025	-	5.065	1.260	0.131
115	1.61	0.315	0.284	0.284	0.115	0.113	0.666	2.722	0.058
116	24.86	0.114	3.133	1.775	0.033	0.024	3.522	1.362	0.263
117	1.67	0.274	0.305	0.235	0.061	0.046	0.592	2.330	0.148
118	1.42	0.222	0.427	0.479	0.094	0.080	1.075	2.492	0.029
119	2.17	0.222	1.268	0.930	0.054	0.053	1.705	1.929	0.013
120	102.00	0.082	3.693	1.780	0.014	-	3.717	1.304	0.206
121	3.44	0.271	0.868	0.960	0.037	0.103	0.444	2.274	0.177
122	3.53	0.273	1.299	1.569	0.058	0.056	0.785	2.011	0.109
123	3.40	0.247	1.130	1.344	0.026	0.023	0.782	1.922	0.175
124	2.61	0.291	0.620	0.745	0.079	0.053	0.418	2.408	0.185
125	14.51	0.060	2.866	2.719	0.103	0.019	4.199	1.286	0.217
126	16.30	0.172	2.824	2.828	0.017	0.063	4.125	1.318	0.199
127	3.10	0.301	0.875	0.906	0.044	0.037	1.202	2.489	0.226
128	3.71	0.200	1.073	1.149	0.108	0.058	1.597	2.441	0.206
129	2.81	0.306	0.517	0.581	0.090	0.048	0.883	1.728	0.146
130	2.57	0.384	0.451	0.547	0.120	0.106	1.103	2.449	0.208
131	4.13	0.279	1.781	1.702	0.040	0.053	3.055	1.759	0.177
132	2.03	0.356	0.469	0.598	0.120	0.071	0.881	2.239	0.082
133	1.88	0.274	0.290	0.423	0.072	0.050	0.732	2.344	0.277
134	2.17	0.243	0.570	0.749	0.113	0.052	1.068	2.610	0.226
135	4.61	0.169	2.034	1.960	0.013	0.046	3.266	1.765	0.260
136	2.82	0.374	0.604	0.691	0.064	0.126	1.105	2.375	0.122
137	2.98	0.362	0.720	0.744	0.107	0.050	1.062	2.456	0.226
138	5.03	0.253	1.994	1.448	0.077	0.087	2.139	1.918	0.115
139	1.41	0.222	0.211	0.427	0.138	0.051	0.820	2.150	0.224
140	1.82	0.305	0.331	0.507	0.104	0.034	0.846	2.259	0.201
141	6.73	0.282	1.796	1.920	0.072	0.033	2.268	1.894	0.188
142	2.55	0.313	0.504	0.603	0.135	0.074	0.854	2.352	0.085
143	3.02	0.291	0.627	0.745	0.104	0.028	0.930	2.252	0.174
144	1.66	0.220	0.481	0.664	0.090	0.053	1.126	2.258	0.131
145	5.27	0.198	2.045	2.077	0.023	0.033	3.254	1.685	0.287
146	1.27	0.196	0.299	0.508	0.081	0.069	0.768	2.164	0.182
147	2.79	0.404	0.622	0.698	0.106	0.069	0.860	2.474	0.054
148	4.04	0.158	1.743	1.709	0.041	0.078	2.820	1.733	0.148
149	5.19	0.182	1.968	2.045	0.010	0.039	3.084	2.253	0.168
150	1.52	0.211	0.321	0.582	0.132	0.065	0.896	2.206	0.093

Table S2. EXAFS parameters from multi-shell fits of Cu-EXAFS data

	Cu-O			Cu-Mn		Cu-Mn		Cu-Mn				
	CN	*R*(Å)	σ(Å^2)	*CN*	*R*(Å)	*CN*	*R*(Å)	*CN*	*R*(Å)	σ(Å^2)	Δ*E*	*Res*
CudBi3-5	4.6	1.94	0.007	0.8	2.87*	1.3	3.40*	0.6	3.68	0.005†	-0.4	9.6
CuTcBi7-6	4.7	1.96	0.007	0.8	2.86	2.3	3.40			0.007†	-2.0	14.1
Diagenetic	4.1	1.96	0.006	1.6	2.88					0.008	-1.6	7.6

Notes: CN is the effective number of atomic pairs seen by EXAFS, *R* is the interatomic distance, σ is the standard

deviation of the distance distribution, ΔE is the threshold energy correction in eV, and *Res* is the fit residual defined as $[\Sigma\{|\chi_{exp} - \chi_{fit}|\}/\Sigma\{|\chi_{exp}|\}] \times 100$. The many body amplitude-reduction factor S_0^2 was fixed to 0.9.
* fixed values.
† Constrained to the same value for all Cu-Mn pairs.

References cited

Bodei, S., Manceau, A., Geoffroy, N., Baronnet, A., and Buatier, M. (2007) Formation of todorokite from vernadite in Ni-rich hemipelagic sediments. Geochimica et Cosmochimica Acta, 71, 5698–5716.

Buatier, M.D., Guillaume, D., Wheat, C.G., Hervé, L., and Adatte, T. (2004) Mineralogical characterization and genesis of hydrothermal Mn oxides from the flank of the Juan the Fuca Ridge. American Mineralogist, 89, 1807-1815.

Chukhrov, F.V., Gorshkov, A.I., Vitovskaya, I.V., Drits, V.A., Sivtsov, A.V., and Rudnitskaya, E.S. (1980) Crystallochemical nature of Co-Ni asbolan. Izvestia Akademia Nauk, SSSR, Seriya Geologicheskaya, 6, 73-81. (Translated in International Geological Review 24, 598-604, 1982).

Drits, V.A., Silvester, E., Gorshkov, A.I., and Manceau, A. (1997) The structure of synthetic monoclinic Na-rich birnessite and hexagonal birnessite. Part 1. Results from X-ray diffraction and selected area electron diffraction. American Mineralogist, 82, 946-961.

Lanson, B., Drits, V.A., Silvester, E.J., and Manceau, A. (2000) Structure of H-exchanged hexagonal birnessite and its mechanism of formation from Na-rich monoclinic buserite at low pH: New data from X-ray diffraction. American Mineralogist, 85, 826-835.

Manceau, A., Gorshkov, A.I., and Drits, V.A. (1992) Structural chemistry of Mn, Fe, Co, and Ni in Mn hydrous oxides. II. Information from EXAFS spectroscopy, electron and X-ray diffraction. American Mineralogist, 77, 1144-1157.

Manceau, A., Lanson, M., and Geoffroy, N. (2007) Natural speciation of Ni, Zn, Ba and As in ferromanganese coatings on quartz using X-ray fluorescence, absorption, and diffraction. Geochimica Cosmochimica Acta, 71, 95-128.

Manceau, A., Marcus, M.A., Grangeon, S., Lanson, M., Lanson, B., Gaillot, A.C., Skanthakumar, S., and Soderholm, L. (2013) Short-range and long-range order of phyllomanganate nanoparticles determined using high energy X-ray scattering. Journal of Applied Crystallography, 46, 193-209.

Manceau, A., Tommaseo, C., Rihs, S., Geoffroy, N., Chateigner, D., Schlegel, M., Tisserand, D., Marcus, M.A., Tamura, N., and Chen, Z.S. (2005) Natural speciation of Mn, Ni and Zn at the micrometer scale in a clayey paddy soil using X-ray fluorescence, absorption, and diffraction. Geochimica et Cosmochimica Acta, 69, 4007-4034.

Takahashi, Y., Manceau, A., Geoffroy, N., Marcus, M.A., and Usui, A. (2007) Chemical and structural control of the partitioning of Co, Ce, and Pb in marine ferromanganese oxides. Geochimica et Cosmochimica Acta, 71, 984-1008.